SYNTHESIS AND CHARACTERIZATIONS OF HYBRID PEROVSKITE $CH_3NH_3PbI_{(3-x)}Cl_x$ SOLAR CELL MATERIAL

Phitsamai   Kamonpha

A Thesis Submitted in Partial Fulfillment of the Requirements for the

Degree of Master of Science in Physics

Suranaree University of Technology

Academic Year 2018

การสังเคราะห์และการหาคุณลักษณะเฉพาะของวัสดุเพอรอฟสไกต์เซลล์แสงอาทิตย์แบบไฮบริดชนิดเมทิลแอโมเนียมเลดไอโอไดด์คลอไรด์

นางสาวพิศมัย กมลภา

วิทยานิพนธ์นี้เป็นส่วนหนึ่งของการศึกษาตามหลักสูตรปริญญาวิทยาศาสตรมหาบัณฑิต
สาขาวิชาฟิสิกส์
มหาวิทยาลัยเทคโนโลยีสุรนารี
ปีการศึกษา 2561

SYNTHESIS AND CHARACTERIZATIONS OF

HYBRID PEROVSKITE $CH_3NH_3PbI_{(3-x)}Cl_x$

SOLAR CELL MATERIAL

Suranaree University of Technology has approved this thesis submitted in partial fulfillment of the requirements for a Master's Degree.

Thesis Examining Committee

Sirichok

_____

(Assoc. Prof. Dr. Sirichok Jungthawan)

Chairperson

Saroj Rujirawat

_____

(Assoc. Prof. Dr. Saroj Rujirawat)

Member (Thesis Advisor)

Rattikorn Yimnirun

_____

(Prof. Dr. Rattikorn Yimnirun)

Member

_____

(Dr. Usa Sukkha)

Member

Narong Chanlek

_____

(Dr. Narong Chanlek)

Member

Kont Chnt

_____

(Assoc. Prof. Flt. Lt. Dr. Kontorn Chamniprasart)

Vice Rector for Academic Affairs

and Internationalization

_____

(Assoc. Prof. Dr. Worawat Meevasana)

Dean of Institute of Science

พิศมัย กมลภา : การสังเคราะห์และการหาคุณลักษณะเฉพาะของวัสดุเพอรอฟสไกต์เซลล์แสงอาทิตย์แบบไฮบริดชนิดเมทิลแอโมเนียมเลดไอโอไดด์คลอไรด์ (SYNTHESIS AND CHARACTERIZATIONS OF HYBRID PEROVSKITE $CH_3NH_3PbI_{(3-x)}Cl_x$ SOLAR CELL MATERIAL) อาจารย์ที่ปรึกษา : รองศาสตราจารย์ ดร.สาโรช รุจิรวรรธน์, 74 หน้า

วัสดุเพอรอฟสไกต์เซลล์แสงอาทิตย์แบบผสมอินทรีย์อนินทรีย์ (Hybrid Perovskite) เป็นวัสดุที่มีความสามารถในการดูดซับพลังงานแสงอาทิตย์ในช่วงความยาวคลื่นของแสงขาวแล้วเปลี่ยนพลังงานแสงอาทิตย์เป็นกระแสไฟฟ้าได้ มีกระบวนสังเคราะห์ที่ง่าย ใช้พลังงานและต้นทุนในการผลิตต่ำ อีกทั้งยังสามารถนำมาประยุกต์ใช้ในวัสดุเซลล์แสงอาทิตย์แบบอื่น ๆ ได้ เช่นนำมาใช้เคลือบบนแผ่นซิลิกอนเพื่อเพิ่มประสิทธิภาพในการดูดกลืนแสงทำให้วัสดุกลุ่มนี้ได้รับความสนใจในฐานะวัสดุกลุ่มใหม่ในกลุ่มพลังงานทางเลือก แต่วัสดุเพอร์รอฟสไกต์ที่สังเคราะห์ได้ยังมีความเสถียรทางโครงสร้างต่ำ จึงเป็นที่สนใจในการศึกษาเกี่ยวกับโครงสร้างของวัสดุเพอรอฟสไกต์แบบผสมอินทรีย์และอนินทรีย์ โดยในขั้นตอนแรกได้พบวิธีการลดเวลาในการเตรียมสารตั้งต้นเมทิลแอโมเนียมไอโอไดด์ (CH_3NH_3I) โดยการเปลี่ยนสารละลายที่ใช้ในการล้างไอโอดีนจากเดิมที่ใช้ไดเมทิลฟอร์มาลดีไฮด์ (DMF) เป็นอะซิโตนในขั้นตอนโซลเจล ซึ่งสามารถลดเวลาในการเตรียมจาก 48 ชั่วโมงเหลือเพียง 12 ชั่วโมง จากนั้นทำการเตรียมผง $CH_3NH_3PbI_3$ และ $CH_3NH_3PbI_{(3-x)}Cl_x$ ด้วยวิธีการปฏิกิริยาของแข็ง แล้วทำการวิเคราะห์คุณลักษณะเฉพาะของโครงสร้างวัสดุเพอรอฟสไกต์ด้วยเทคนิคต่าง ๆ และจากผล XRD และ XAS ที่ได้จากการทดลองเราพบว่าคลอไรด์ไม่สามารถแทนที่ไอโอไดด์ในโครงสร้างเพอรอฟสไกต์จากการเตรียมด้วยวิธีการดังกล่าวได้

สาขาวิชาฟิสิกส์ ลายมือชื่อนักศึกษา_____
ปีการศึกษา 2561 ลายมือชื่ออาจารย์ที่ปรึกษา_____
ลายมือชื่ออาจารย์ที่ปรึกษาร่วม_____
ลายมือชื่ออาจารย์ที่ปรึกษาร่วม_____

PHITSAMAI KAMONPHA : SYNTHESIS AND
CHARACTERIZATIONS OF HYBRID PEROVSKITE
$CH_3NH_3PbI_{(3-x)}Cl_x$ SOLAR CELL MATERIAL
THESIS ADVISOR : ASSOC. PROF. SAROJ RUJIRAWAT, Ph.D.
74 PP.

HYBRID PEROVSKITE/X-RAY ABSORPTION SPECTROSCOPY

The emerging of perovskite solar cell has attracted many interests in the synthesis and characterization of hybrid perovskite materials related to methylammonium iodide CH_3NH_3I (MAI) due to various interesting properties. In this work, we found a faster way to synthesis hybrid perovskite $MAPbI_3$ from MAI precursor is reported. Which can be shortened by a factor of four, from 48 h to 12 h by changing the reduction agent from dimethylformamide (DMF) to acetone. The MAI precursors from acetones were used to synthesis hybrid perovskite $MAPbI_3$ and $MAPbI_{(3-x)}Cl_x$ (x=0,1,2) powders by solid state method. Finally, the characterization of MAI , $MAPbI_3$ and $MAPbI_{(3-x)}Cl_x$ powder by X-ray Diffraction (XRD), Infrared Spectroscopy(IR) and X-ray Absorption Spectroscopy (XAS) showed that the characteristic of hybrid perovskite $MAPbI_3$ and $MAPbI_{(3-x)}Cl_x$ powders from acetone and DMF are comparable thus confirm the effectiveness of the new preparation route. From XRD and XAS, we found that Cl cannot substitute for I in X side of perovskite structure (ABX_3) using solid state method.

School of Physics	Student's Signature _Phitsamai Kamonpha._
Academic Year 2018	Advisor's Signature _Saroj Rujirawat_
	Co-advisor's Signature _Rattchadon Yimnirun_
	Co-advisor's Signature _____

ACKNOWLEDGEMENTS

Phitsamai Kamonpha

CONTENTS

CONTENTS (Continued)

CONTENTS (Continued)

LIST OF TABLES

LIST OF TABLES (Continued)

LIST OF FIGURES

LIST OF FIGURES (Continued)

LIST OF FIGURES (Continued)

LIST OF FIGURES (Continued)

LIST OF FIGURES (Continued)

LIST OF FIGURES (Continued)

LIST OF ABBREVIATIONS

EDX   Energy Dispersive Spectroscopy

EXAFS   Extended X-ray Absorption Fine Structure

FEFF   Effective Scattering Amplitude

FMS   Full-Multiple Scattering

FWHM   Full Width at Half Maximum

IR   Infrared Spectroscopy

PCE   Power Conversion Efficiency

SCF   Self-Consistent Field

SEM   Scanning Electron Microscope

SLRI   Synchrotron Light Research Institute

XANE   X-ray Absorption Near Edge Structure

XAS   X-ray Absorption spectroscopy

XPS   X-ray Photoelectron Spectroscopy

XRD   X-ray Diffraction

CHAPTER I

INTRODUCTION

1.1   BACKGROUND

Currently, electrical power is increasingly more important for human than ever and it is expected that the future demand for electricity will be increasing more. The trend of world energy consumption by energy source is shown in Figure.1.1. In the past, the most of energy has come from burning fuels such as wood, coal, oil and natural gas, so if we use of these resources for generating electricity, they will cause a greenhouse gas due to the carbon dioxide gas from burned fuel increase and led to global warming. So, renewable energy sources such as biomass, wind, hydropower and led to global warming. So, renewable energy sources such as biomass, wind, and hydropower and solar for generating electricity became attractive because they are environmentally friendly and generated less greenhouse gases. Solar energy is a good choice of renewable energy with plentiful of energy source from the nuclear reaction within the sun. In this work, we focus on material for photovoltaic solar cell for electricity production which is green energy and sustainable. Photovoltaic cells or PV cells are devices for harvesting solar energy and converting it to electricity. The most ordinary material for solar panel production is crystalline silicon which has semiconductor properties. There are four main types of solar panels commercially. available: (1) monocrystalline silicon PV, (2) polycrystalline silicon PV, (3) amorphous silicon PV, (4) hybrid PV (Administration, 2015). Researchers at National Renewable Energy Laboratory (NREL) reported world record one-sun efficiencies of 32.8% for dual-junction GaInP/GaAs

solar cell devices, and the dual-junction device with mechanically stacked silicon solar cells, to achieve a record one-sun efficiency of 35.9% for triple-junction solar cells (figure 1.2).(Essig et al., 2017). Perovskite solar cells became popular recently.
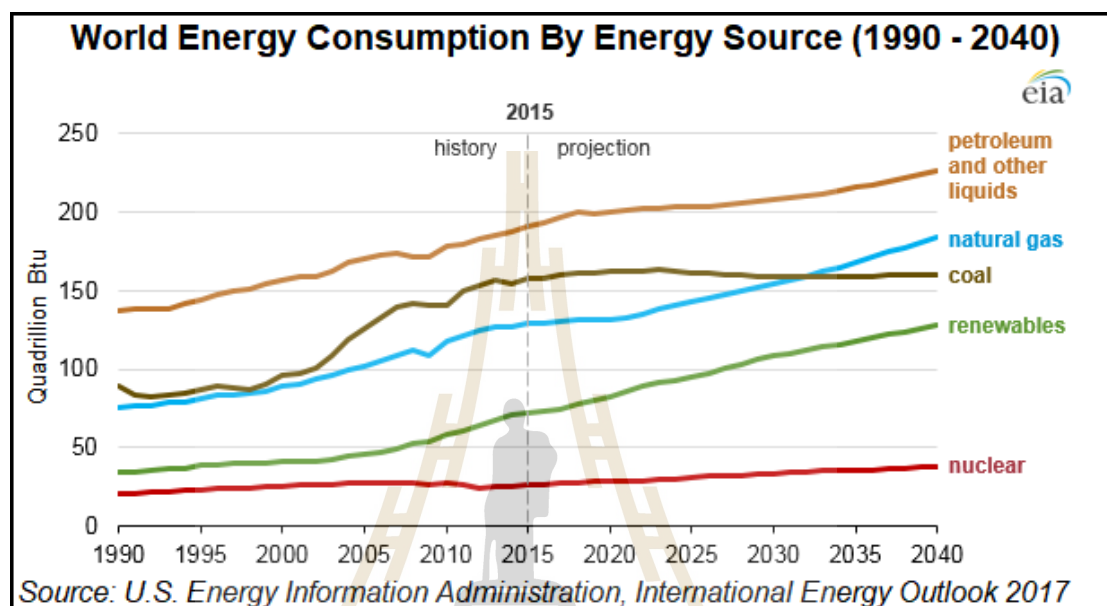
Figure 1.1 World energy consumption by energy source. (Administration, 2015)

Organic-inorganic lead halide perovskites is a photovoltaic material that exhibits high power conversion efficiency (PCE) because of their strong light absorption band across solar spectrum (figure 1.3) and long free carrier diffusion length of few microns. Yanbo Li reported high-efficiency planar $CH_3NH_3PbI_{(3-x)}Cl_x$ (Compared with films derived from mixed $PbI_2/PbCl_2$ precursors) perovskite photovoltaics, of 16.8% with highly repeatable (Yu et al., 2014). The performance without any need for a mesoporous or nanocrystalline metal oxide layer (Li et al., 2015). A variety of reports have suggested that Cl enables long photocarrier lifetimes, increases diffusion lengths in halide perovskite materials, and as well as low working temperature. John A. Mc Leon reported that Methyl ammonium lead trihalide ($CH_3NH_3PbI_{(3-x)}Cl_x$) perovskite, usually synthesized from two precur-
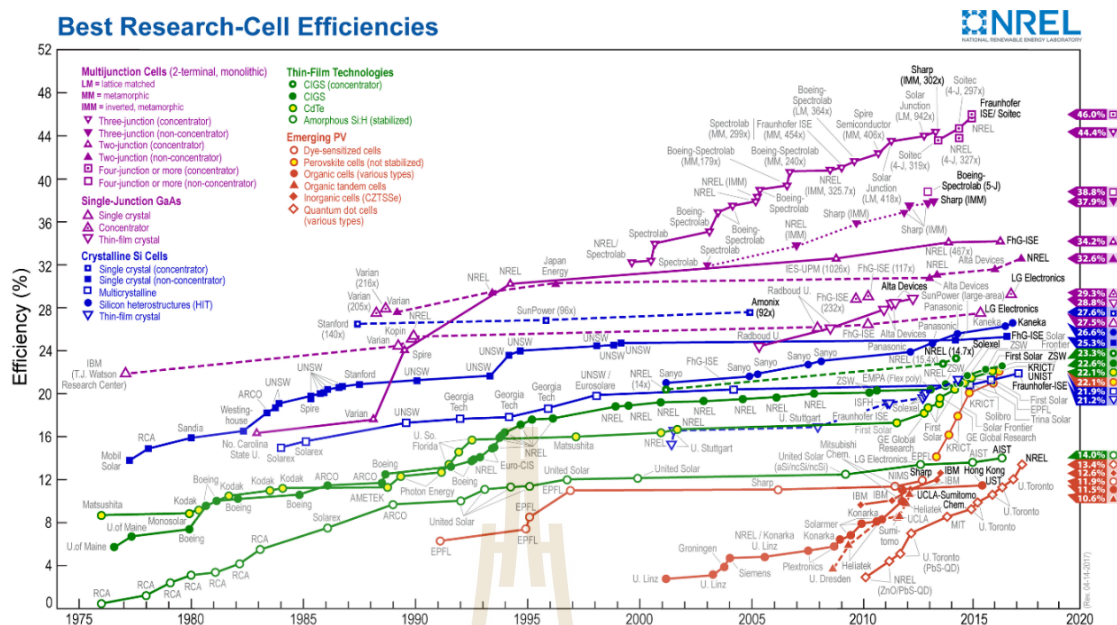
Figure 1.2 Reported timeline of solar cell energy conversion efficiencies (Elseman et al., 2018).

sors, CH_3NH_3I and $PbCl_2$ at a ratio of 3:1 with slight adjustment of I/Cl ratio in the precursor mixture plays a strong effect on solar cell performance. An in-depth chemical study about the possible impurities formed during CH_3NH_3I preparation was presented and their relevance on solar cell processing is revealed (McLeod et al., 2016). HI was shown to effect iodide coordination. There was a strong correlation between the lead coordination chemistry in precursor solutions and the surface coverage and morphology of the resulting $MAPbI_3$ film (Sharenko et al., 2017). Impurities can give rise to the better perovskite solar cell devices, compared with impurity-free precursor (Levchuk et al., 2016).

In this work, we will synthesize CH_3NH_3I (MAI) by Sol-gel method using different solvents, to optimize the synthesis time. The synthesis MAI will be characterized to find morphology, functional group, and chemical composition using X-ray Diffraction (XRD), Infrared Spectroscopy (IR) and X-ray absorption spectroscopy (XAS), respectively. Next, the solar cell perovskite materials
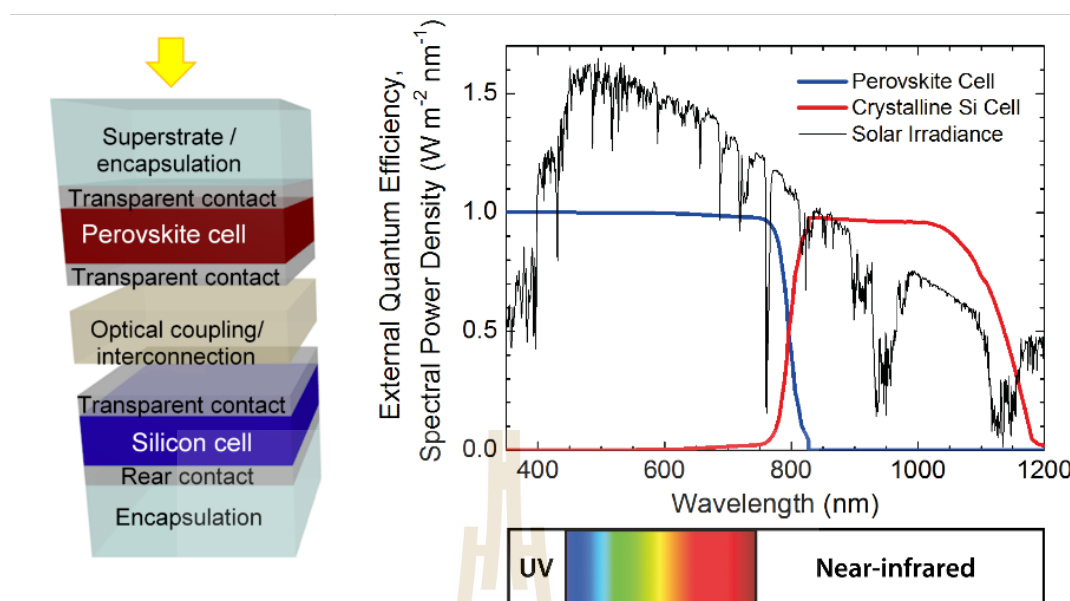
Figure 1.3 Solar radiation spectrum.

$CH_3NH_3PbI_{(3-x)}Cl_x$ will be synthesized using solid-state method from CH_3NH_3I and $PbCl_2$ precursors. $PbCl_2$ precursor will be used to substitute Cl for I in $CH_3NH_3PbI_3$ to improve thermal stability and devices lifetime. After synthesis $CH_3NH_3PbI_{(3-x)}Cl_x$ will be analyzed to find the structure, size, and morphology by x-ray diffraction (XRD) and Scanning electron microscope (SEM). The chemical composition, local structure and electronic structure will be studied by Energy-dispersive X-ray spectroscopy (EDX), Infrared spectroscopy (IR), X-ray absorption spectroscopy (XAS) and X-ray photoelectron spectroscopy (XPS).

1.2   REVIEW OF LITERATURES

1.2.1   Structure of perovskite

Perovskite is named of Russian mineralogist Count Lev Alekseevich perovski (1792-158) and discovered by Gustav Rose in 19th century in Ural Mountains of Russia. The name of perovskite refers to all material with the same crystal

structure as calcium titanium oxide or calcium titanate ($CaTiO_3$). The general chemical formula of perovskite is ABX_3. In this formula 'A' and 'B' are to cation of different sizes (A cation are larger than the B cation.), and 'X' is an anion that bonds to 'A' and 'B' cation. The 'A' cation is an alkaline earth or rare earth element as Cesium, Calcium and Natrium (In type of hybrid perovskite or organic-inorganic perovskites, A is methylammonium (MA) or Formamidine (FA), The 'B' cation could be a 3d,4d or 5d transition metal as Ti ,Pb, Sn and Fe. And X anion is halogen group e.g. O, Cl, Br and I.

The crystallography of perovskite can be represented in multiple ways. The simplest way to think about a cubic structure and 'A' cations are positioned in corner, 'B' cations at the body center and 'X' anions at face center of the perovskite cube structure. The second way a large atomic or 'A' cations (positively charged) in the center of a cube. The corners of the cube are occupied by 'B' cation (also positively charged cations) and the faces of the cube are occupied by a smaller atom X with negative charge (anion). Crystal of perovskite could be black, brown, gray and orange to yellow color. These crystals appear as cubes, but they are actually pseudo cubic.

1.2.2 Organo-Metal halide perovskites

We focus on a hybrid perovskite based on organic-inorganic trihalide perovskites. From the figure 1.6 organic-inorganic trihalide perovskites is one of kind perovskite in halide group. They have chemical formula ABX_3, where A is an organic group the methylammonium (CH_3NH_3) (MA) or formamidine [$HC(NH_2)_2$] (FA) cation, B is commonly lead (Pb) and X is a halide (Cl, Br, or I). methylammonium lead halide ($MAPbX_3$, where MA is methylammonium CH_3NH_3 and X is a halogen) perovskites have good absorber for visible light because they are very
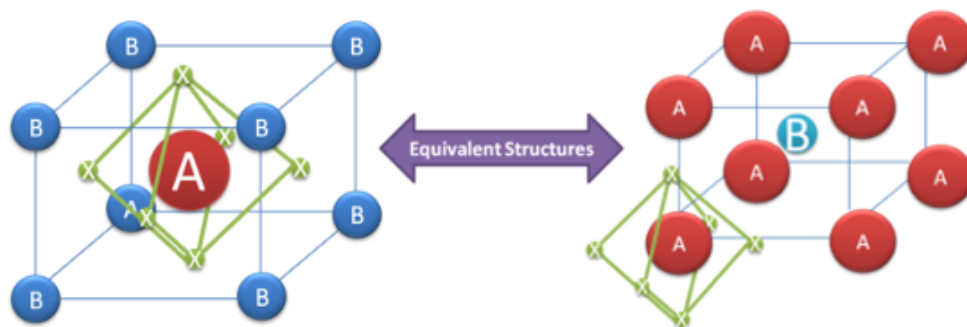
Figure 1.4 A generic perovskite crystal structure of the form ABX_3. Note that the two structures are equivalent – the left-hand structure is drawn so that atom B is at the $< 0,0,0 >$ position while the right-hand structure is drawn so that atom (or molecule) A is at the $< 0,0,0 >$ position. Also note that the lines are a guide to represent crystal orientation rather than bonding patterns.
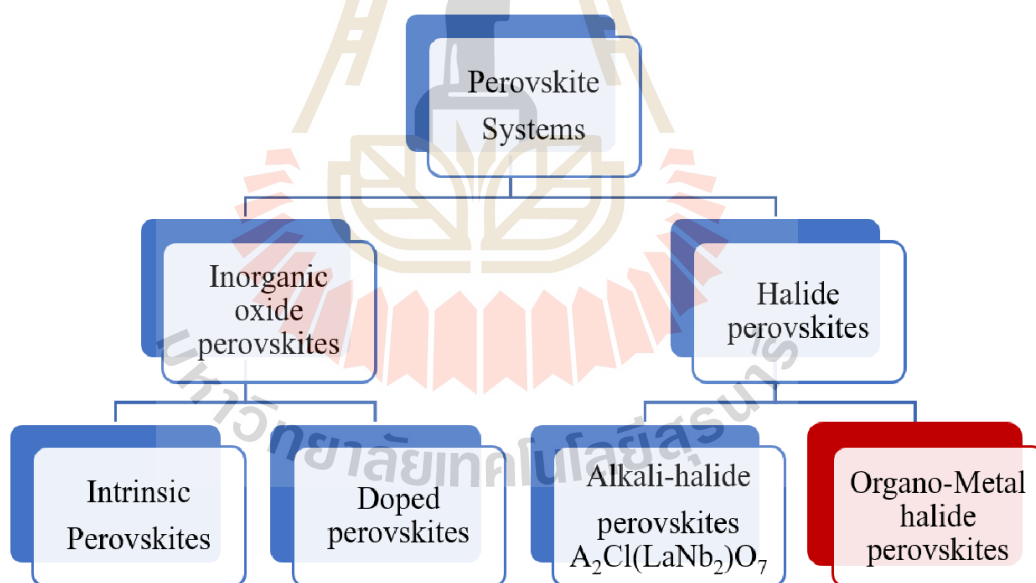
Figure 1.5 Classification of perovskite system.

well of managing chemical compositions, ambipolar charge transport, and very long electron-hole discussion lengths so they are very good of optical properties. M. A. Green et al, present about organometallic halide perovskites is a kind of

perovskite structural crystalline materials are consisting of organic methylamine and inorganic lead halide, it's rapidly become promising semiconductors for solar cell applications and can increase the power conversion efficiencies from less than 4% in 2009 to over 20% now for methylammonium lead iodide ($CH_3NH_3PbI_3$) (Green et al., 2015). Owing to $CH_3NH_3PbI_3$ have a band gap of 1.55-1.60 eV. In addition, perovskite materials can have applied to light absorbers in thin or thick mesoscopic metal oxides and planar heterojunction solar devices.
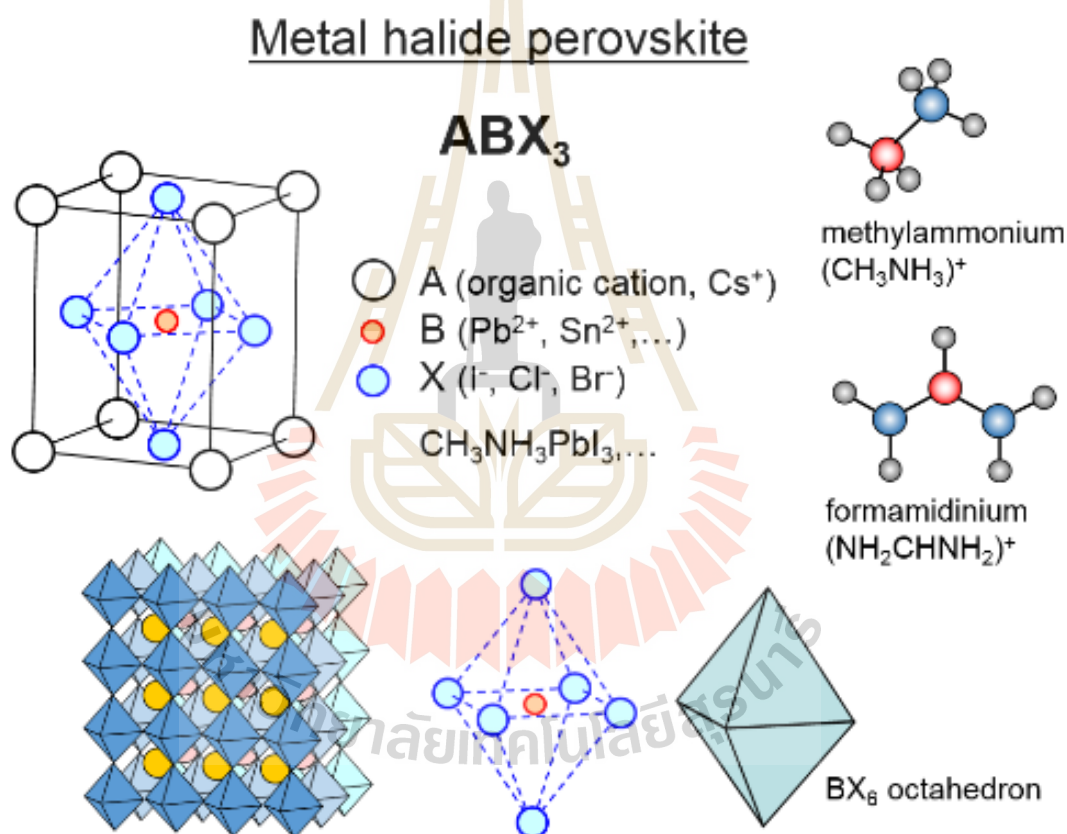
Figure 1.6 A generic Organo Metal halide perovskite crystal structure.

From ABX_3 in figure1.6 we will be varying the X site, one group has found that using small chloride ions rather than large iodides improves stability. Jarvis M. Frost represent about compared electrostatic lattice energy and site Madelung potentials for a range of ABX_3 perovskite structures (Cubic lattice, a = 6.00 Å)

assuming the formal oxidation state of each species. They found group VII anions are the electrostatic stabilization and the lattice energy increases as the charge imbalance between A and B sites is removed more than VI anions due to the group VII or halide are weak bonding, less-confining, potential, lower ionization potentials (work functions), when they compared with metal oxides. And for X they use halide group for balance cation, as demonstrated in the series of hybrid structures with lower dimensionality in the inorganic networks. For layered structures, the crystal properties become highly anisotropic (Frost et al., 2014). Yanbo Li reported about a new method for achieving high efficiency planar $CH_3NH_3PbI_{(3-x)}Cl_x$ perovskite photovoltaics by annealing and exposure to CH_3NH_3I vapor at low pressure for comparison with films derived from mixed $PbI_2/PbCl_2$ precursors.

Table 1.1 Device performance of perovskite solar cells. ([a] standard derivation calculated on 8 devices. [b] standard derivation calculated on 32 devices.)

Formula	$J_{SC}(mA/cm^2)$	$V_{OC}(V)$	FF	PCE(%)
$MAPbI_3$(average)[a]	20.9±0.4	1.00±0.01	0.68±0.01	14.2±0.3
$MAPbI_{(3-x)}Cl_x$(best)	21.7	1.04	0.75	16.8
$MAPbI_{(3-x)}Cl_x$(average)[b]	21.3±0.6	1.00±0.02	0.73±0.02	15.7±0.07

Therefor chloride (Cl) enables long photocarrier lifetimes and increased diffusion lengths in halide perovskite materials, it's summarized in table 1.1 And the heterojunction devices based on this hybrid halide perovskite exhibit a top PCE of 16.8%. And found chloride can be a success photoluminescence lifetime which was enhanced by nearly an order of magnitude and an improved power conversion efficiency from 13% to 15.3% and 16.5% after treated solar cells by thiophene and pyridine, respectively (Noel et al., 2014). From the table1.1 they mixed halide perovskite phase crystalline $CH_3NH_3PbI_{(3-x)}Cl_x$ gives the best device performance.

It can alter the band gap, giving both electron and hole diffusion lengths more than 1 μm, compared with the effective diffusion length of $CH_3NH_3PbI_3$ for holes but a shorter one for electrons (Stranks et al., 2013). The extra-long carrier diffusion length is contributed to the better efficiency of the solar cell, so we can have improved device performance by doped chloride in a crystal structure, and $CH_3NH_3PbI_{(3-x)}Cl_x$ is found to possess an almost identical crystal structure and electronic structure as $CH_3NH_3PbI_3$ as characterized by X-ray diffraction (XRD) and X-ray photoelectron spectroscopy (XPS) (McLeod et al., 2016).
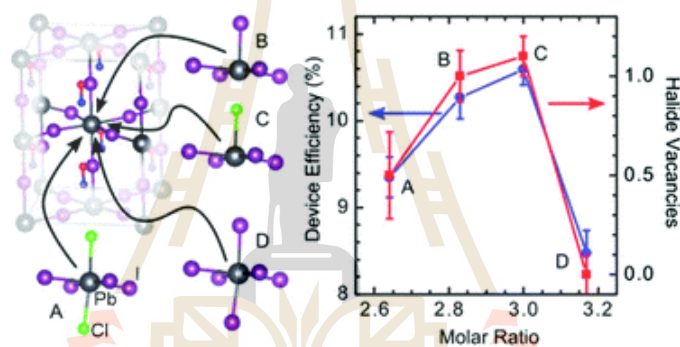
Figure 1.7 Structures of Pb coordinated by I, Cl, nearby CH_3NH_3 and The PCEs of the devices (blue), the number of halide vacancies from EXAFS fitting (red).

The Cl replaced on I in crystal structure of perovskite not clear that what reason bring about increasing of PCE, but it can be used to explain why $CH_3NH_3PbI_3$, if used as an absorber in a flat design (i.e., without mesoporous scaffold), has efficiencies of 2–3%, while with $CH_3NH_3PbI_{(3-x)}Cl_x$ nearly 16% can be reached. Furthermore, structure of perovskite about Cl substitute I in perovskite that was reported by J. A. McLeod. about the influence of I/Cl ratio on the performance of $CH_3NH_3PbI_{(3-x)}Cl_x$ based solar cells and found the crystal structure of $CH_3NH_3PbI_{(3-x)}Cl_x$ formed from CH_3NH_3I and $PbCl_2$ precursors with molar ratios of 2.64:1, 2.83:1, 3.0: and 3.17:1. They found Structures of Pb

coordinated by I, Cl, nearby CH$_3$NH3 and after change ratio of CH$_3$NH$_3$I and PbCl$_2$, the films with lower ratios have lower PCEs, they still exhibit many of the same structural and electronic properties as the ideal 3:1 perovskites and at the ratio 3:1 are the highest PCE (shown in figure1.6 and table 1.2). In this work, we choose to study CH$_3$NH$_3$PbI$_{(3-x)}$Cl$_x$ in the molar ratio of 3:1.

Table 1.2 Electrical output characteristics of the devices with perovskite films with different CH$_3$NH$_3$I/PbCl$_2$ ratios under light at stimulated AM 1.5 solar illumination at 100 mW cm^{-2}. V$_{OC}$: open circuit voltage, J$_{SC}$: short circuit current density, FF: fill factor.

CH$_3$NH$_3$I/PbCl$_2$	V$_{OC}$(V)	J$_{SC}$(mA/cm^2)	FF	PCE(%)
2.64:1	0.96 $\pm$ 0.01	15.35 $\pm$ 0.23	0.64 $\pm$ 0.03	9.35 $\pm$ 0.23
2.83:1	0.90 $\pm$ 0.01	16.60 $\pm$ 0.18	0.69 $\pm$ 0.02	10.27 $\pm$ 0.25
3.00:1	0.94 $\pm$ 0.01	17.07 $\pm$ 0.26	0.69 $\pm$ 0.02	10.59 $\pm$ 0.18
3.17:1	0.96 $\pm$ 0.01	13.96 $\pm$ 0.64	0.61 $\pm$ 0.03	8.47 $\pm$ 0.27

After study literature about perovskite, such as effect from the compound is consist in the crystal structure, temperature and time to annealing, the process to synthesize and fabricated device. We interested to study properties of perovskite structure from different temperature and times for annealing. Then in this work we will prepare material by the sol-gel and solid-state method due to Sol-gel method is a method for producing solid materials from small molecules. The method is used for the fabrication of metal oxides, the process involves conversion of monomers into a colloidal solution (sol) that acts as the precursor for an integrated network (or gel) of either discrete particles or network polymers and solid-state reaction is a chemically react without the presence of any solvent at high temperatures yielding a product which a stable, both method is easy to synthesize and appropriate for

produce powder of perovskite. In sol-gel method, we will vary the solution for reduced iodide (I_2) from CH_3NH_3I salt by different type because we want a powder product for following next step.
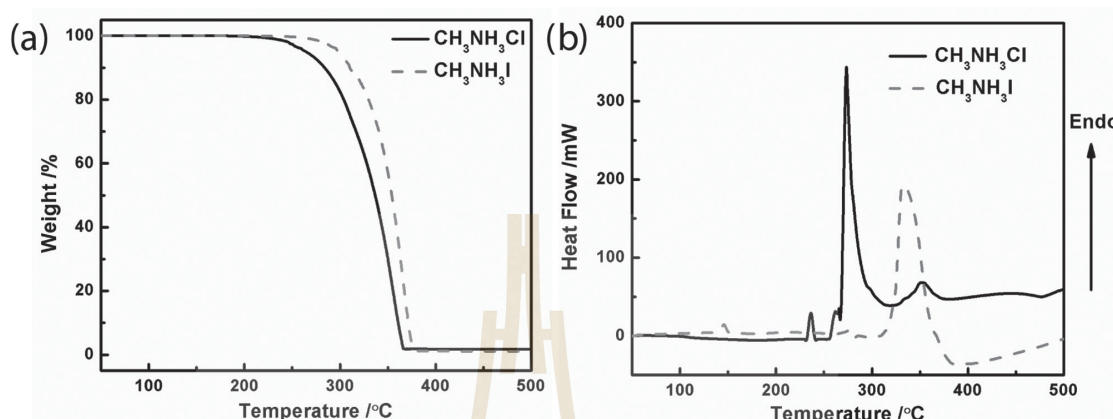
Figure 1.8 a) TGA and b) DSC curves for CH_3NH_3I and CH_3NH_3Cl powders (Zhang et al., 2014).

Table 1.3 Temperature for annealing and PCE of materials (Liu et al., 2015), (Noel et al., 2014), (Jeon et al., 2014), (Shao et al., 2014), (Yu et al., 2014), (Zhang et al., 2014), (Li et al., 2015).

Formula	Temperature(°C) for annealling	Times (minutes)	PCE(%)	Methods
$MAPbI_{(3-x)}Cl_x$	140	20	10.5	Sol-gel& spin costing
$MAPbI_{(3-x)}Cl_x$	90	180	$13 \rightarrow 15$	Sol-gel& spin costing
$MAPbI((1-x)Br_x)_3$	100	10	16.2	Sol-gel& spin costing
$MAPbI_3$	110	20	15.6	Sol-gel& spin costing
$MAPbI_{(3-x)}Cl_x$	100,130,150*	50,20,20 *	12*	Sol-gel& spin costing
$MAPb(I,Br,Cl)_3$	100	30	16	Sol-gel& Solid State
$MAPbI_{(3-x)}Cl_x$	120	120	15.7	Sol-gel& spin costing

We unnecessary to dissolve salt of CH_3NH_3I. After finished in the sol-gel method we prepared the compound of $CH_3NH_3PbI_{(3-x)}Cl_x$ by the solid-state method and followed by annealing at a different temperature. The temperature for annealing we reference by TGA and DSC (figure 1.8) and summarized from literature review about synthesis perovskite on table 1.3 Then, from data in table 1.3 and figure 1.8, we will should temperature to annealing in range of 100 - 250 °C at 30-120 minutes for synthesis crystal structure.

1.2.3 Phases and optical of hybrid perovskite

In general features of hybrid perovskite, they have a different phase in differences temperature with the cubic phase at a high temperature and the Tetragonal phase being the stable phase at room temperature and the Orthorhombic phase at a low temperature. The crystal structure of of organic- halide perovskite shows in table 1.4. And in Figure 1.9 shows the three initial simple cubic structures and phase transition of $MAPbI_3$ perovskite. The transition from cubic to tetragonal happened at very low temperature around 330 Kelvin degrees. which is a temperature reached during the salvation process.
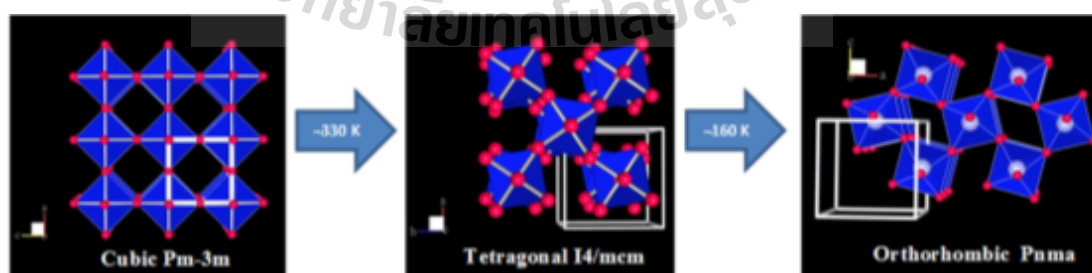
Figure 1.9 Phase transition of $MAPbI_3$ perovskite.

The brillouin zone of simple cubic structure is shown in Figure 1.10 To draw all the K point for simple cubic structure, it must draw from C point

Table 1.4 Crystal structures of $CH_3NH_3PbX_3$ (X=Cl, Br, I) (Oku, 2015).

Material	$CH_3NH_3PbCl_3$	$CH_3NH_3PbBr_3$	$CH_3NH_3PbI_3$
Crystal system	Cubic	Cubic	Cubic
Transition temperature(K)	177	236	330
Crystal system	Tetragonal	Tetragonal	Tetragonal
Transition temperature(K)	172	149 154	161
Crystal system	Orthorhombic	Orthorhombic	Orthorhombic

(Gamma, this calculation abbreviated to G), to M, R, G, X, M, G, R, X points. The energies of $MAPbBr_3$, $MAPbI_3$ and $MAPbCl_3$ increase 1.34, 1.52 and 2.26 eV, respectively. large bandgap is used for short wavelength (blue/violet) , and small bandgap for long wavelength.
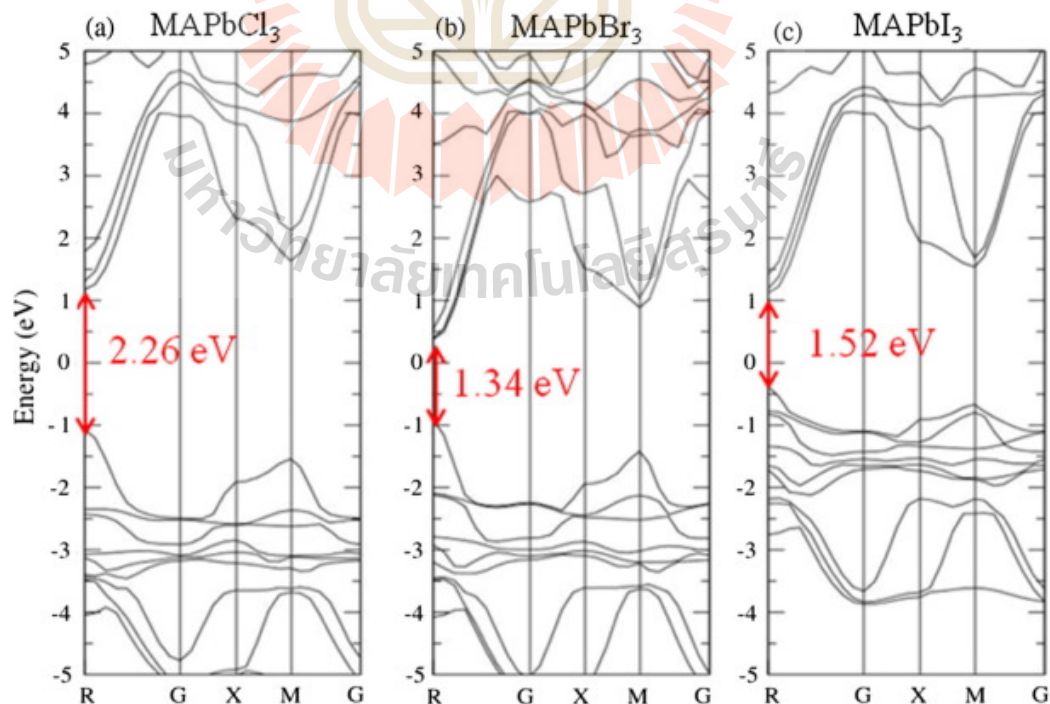
Figure 1.10 E-k diagram of $MAPbX_3$ (Pan et al., 2016).

1.3 RESEARCH OBJECTIVES

The objectives of this research are as follows:

1.3.1 To examine the possibility of synthesizing $CH_3NH_3PbI_{(3-x)}Cl_x$ compound.

1.3.2 To characterize the synthesized $CH_3NH_3PbI_{(3-x)}Cl_x$ compound using advanced characterization tools.

1.3.3 To study the optical properties of the $CH_3NH_3PbI_{(3-x)}Cl_x$ compound by light absorber technique.

1.3.4 To investigate other properties of the synthesized $CH_3NH_3PbI_{(3-x)}Cl_x$ compound in relation to its application in solar cells.

1.4 SCOPE AND LIMITATIONS

1.4.1 This study focuses on the synthesis of CH3NH3I compound by sol-gel method and preparation of $CH_3NH_3PbI_{(3-x)}Cl_x$ compound by solid-state reaction method.

1.4.2 The phase identification, structure characterization and the effect of temperature on the synthesized compound will be investigated using XRD to look at the structure of the compound and, IR Spectroscopy, TG-DTA techniques.

1.4.3 The chemical state and electronic state of the synthesized $CH_3NH_3PbI_{(3-x)}Cl_x$ compound will be investigated using the XPS and XAS technique.

CHAPTER II

RESEARCH METHODOLOGY

2.1 SYNTHESIS

2.1.1 Precursor preparation and CH_3NH_3I analysis

CH_3NH_3I was synthesized in an ice-water bath condition (0°C) for 2 hrs. by reacting methylamine (CH_3NH_2, 40 wt.% aqueous solution) with hydroiodic acid (HI, 57 wt.% aqueous solution), slowly add hydroiodic acid to methylamine.After we mixed HI and methyaminein ice bath, we heat the mixture to 50°C. And got sero-gel after heating at 50°C around 8 hrs. We washed a sero-gel for several times with Acetone after that we separate they into 2 part. For drying in air at room temperature and for drying at 60°C in Ar. And in this process, we found CH_3NH_3I washed by acetone and dry in Ar have a stability than CH_3NH_3I washed by acetone and dry in Air.
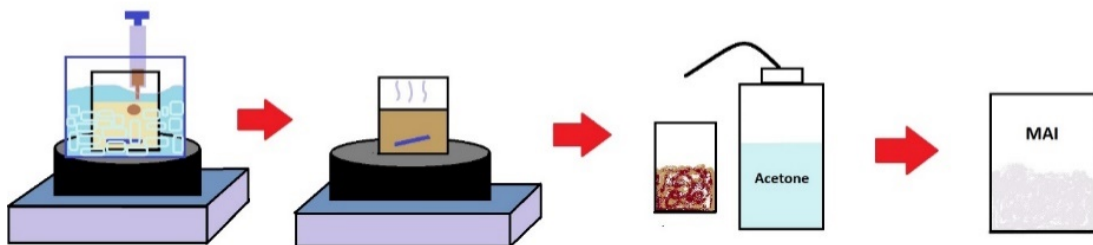
Figure 2.1 Schematic of sol-gel method.

The stability of CH_3NH_3I depend on moisture, oxygen, and UV radiation. Interaction in the decomposed process shows in the equilibrium of reaction (1)-(3) leads to the co-existence of CH_3NH_3I, CH_3NH_2, and HI in the powder.

(1) CH_3NH_3I (aq) $\rightleftharpoons$ CH_3NH_2 (aq) + HI (aq)

(2) $4HI$ (aq) + O_2 (g) $\rightleftharpoons$ $2I_2$ (s) + $2H_2O$ (l)

(3) $2HI$ (aq) $\rightleftharpoons$ H_2 (g) + I_2 (s)
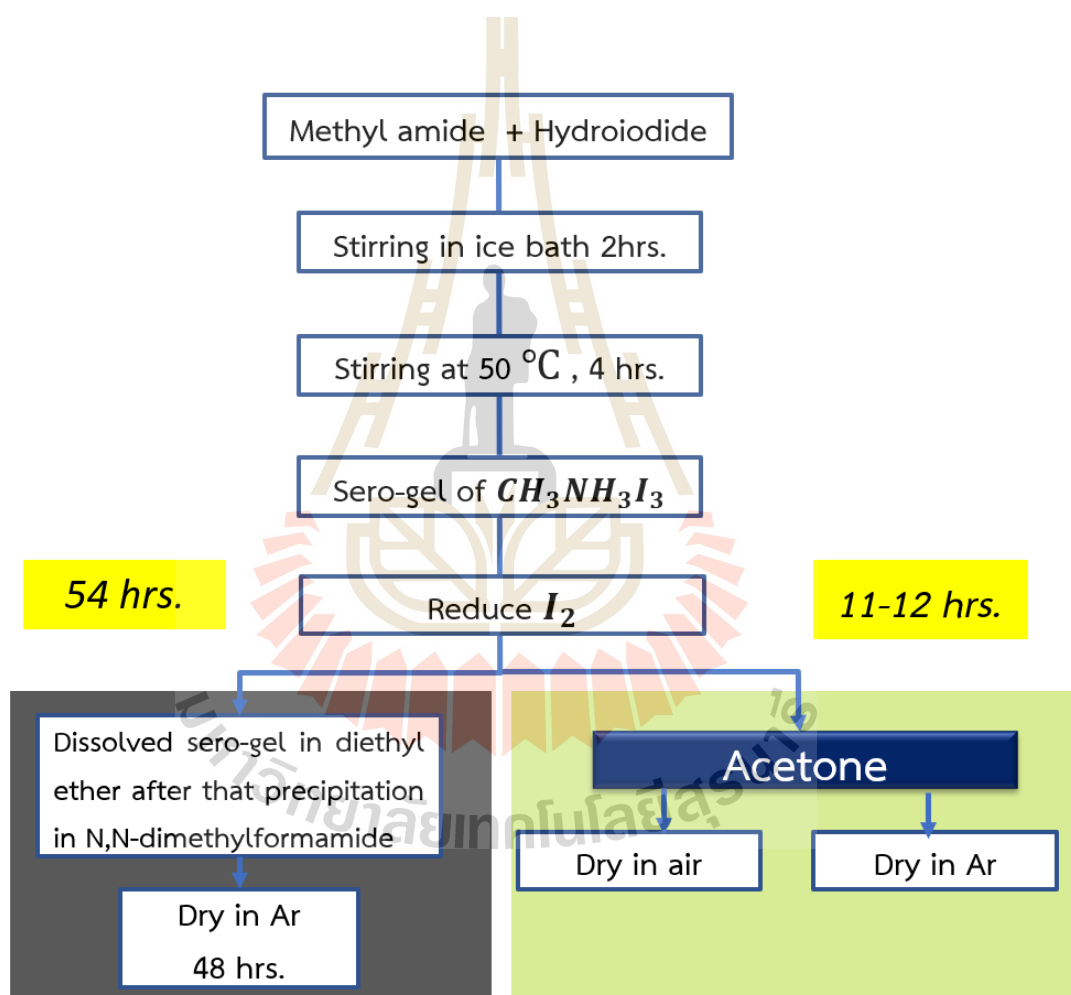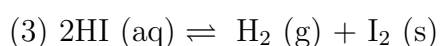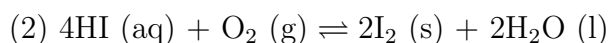
Figure 2.2 Schematic diagrams for CH_3NH_3I preparation.

The color change of CH_3NH_3I under different conditions process demonstrated that only air and UV radiation could lead to the brown color, which is due to the existence of I_2 (Niu et al., 2015).
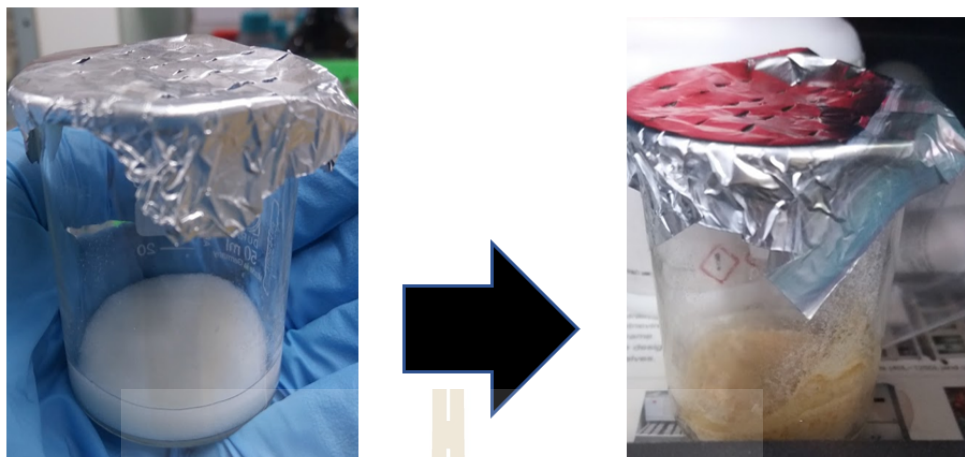
Figure 2.3 The redox reaction of CH$_3$NH$_3$I.

2.1.2 Preparation CH$_3$NH$_3$PbI$_3$ and CH$_3$NH$_3$PbI$_{(3-x)}$Cl$_x$ analysis

The mixed halide perovskite (CH$_3$NH$_3$PbI$_3$) were prepared in nitrogen-filled glovebox by solid state method a precursor solution of CH$_3$NH$_3$I and PbI$_2$ at a 1:1 molar ratio, followed by thermal annealing at different temperatures and times. And CH$_3$NH$_3$PbI$_{(3-x)}$Cl$_x$ powder were prepared in nitrogen-filled glovebox by solid state method a precursor solution of CH$_3$NH$_3$I and PbCl$_2$ at a 3:1, 2:1, 1:1 molar ratio, followed by thermal annealing at different temperatures and times.
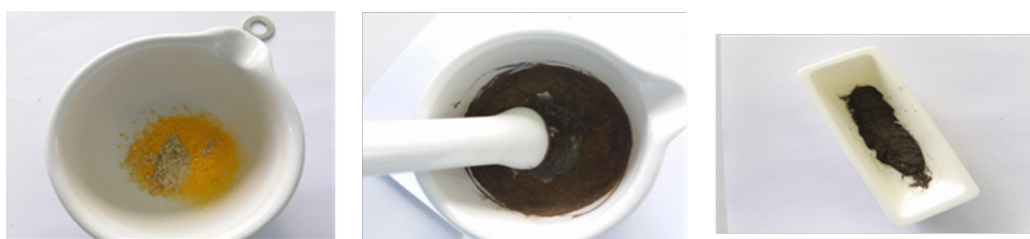
Figure 2.4 Solid state method.
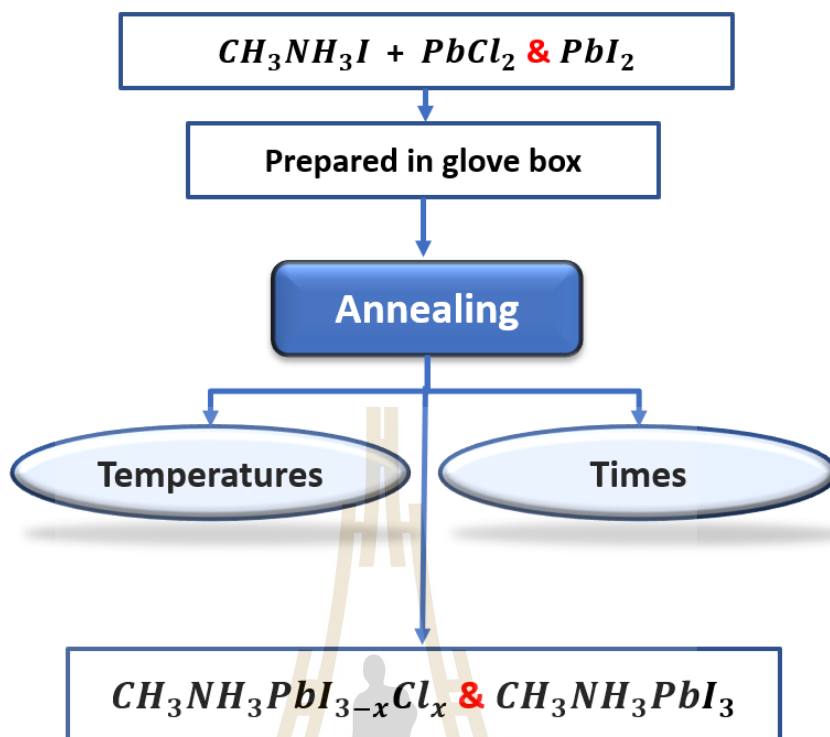
Figure 2.5 Schematic diagrams for $(CH_3NH_3PbI_3$ and $(CH_3NH_3PbI_{(3-x)}Cl_x)$ preparation.

2.1.3 Devices

We prepared perovskite devices by spin-coating process and preparation substrate follow schematic in figure 2.6. After we prepared substrates. We are creating perovskite film as follow. First, a mixture of $CH_3NH_3PbI_3$, GBL and DMSO in the appropriate ratio is spread over the entire surface of the substrate. Second, the spin-coater is accelerated to the desired rotational speed and maintained there for several tens of seconds to evaporate the solvent. Third, a solvent that does not dissolve the perovskite materials and is miscible with DMSO and GBL (for example, toluene or chloroform) dripped on the substrate during spinning. Fourth, all constituents are frozen into a uniform layer on the removal of the residual DMSO and then a new complex as an intermediate phase is formed (see in figure 2.7).

Finally, the complex is converted into highly uniform and crystalline perovskite on annealing at 100°C for 10 minutes.
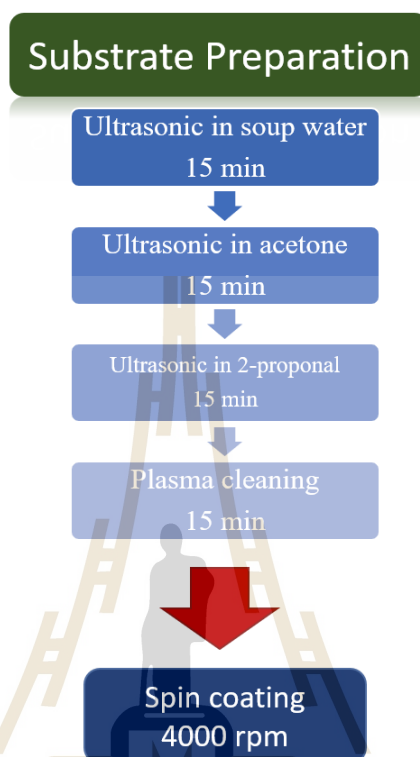
Figure 2.6 Schematic of prepared film method.

Figure 2.7 The precusor for prepared $CH_3NH_3PbI_3$, $CH_3NH_3PbI_{(3-x)}Cl_x$. And film after annealing.

2.2   CHARACTERIZATION

2.2.1   X-Ray Diffractometer (XRD)

X-ray diffraction analysis (XRD) is a common analytical technique for study phase identification of crystalline materials form breakage faces of samples and can provide information on unit call dimensions.
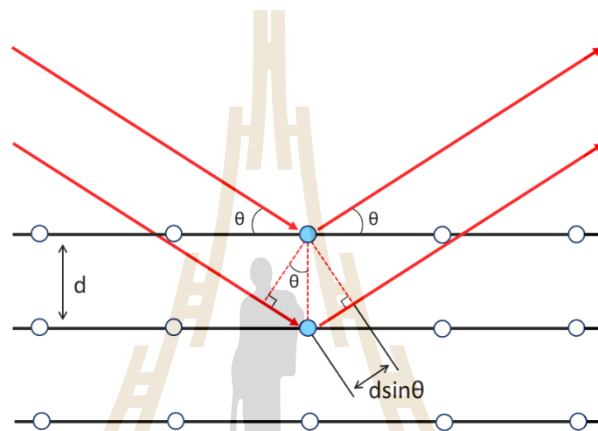
Figure 2.8 Bragg diffraction. Two beams with identical wavelength and phase approach a crystalline solid and are scattered off two different atoms within it. The lower beam traverses an extra length of $2d\sin\theta$. Constructive interference occurs when this length is equal to an integer multiple of the wavelength of the radiation.

The X-ray diffraction methods was start from generate X-ray by a cathode ray tube, filtered to produce monochromatic radiation, collimated to concentrate, and directed toward the sample. When the detector moves in a circle around the sample, X-ray waves incident on an atom of sample, the X-ray waves are scattered from lattice planes and produces constructive interference from a separated of waves in the interplanar distance d. The detector will be recording the number of X-ray by observed at each angle 2θ.
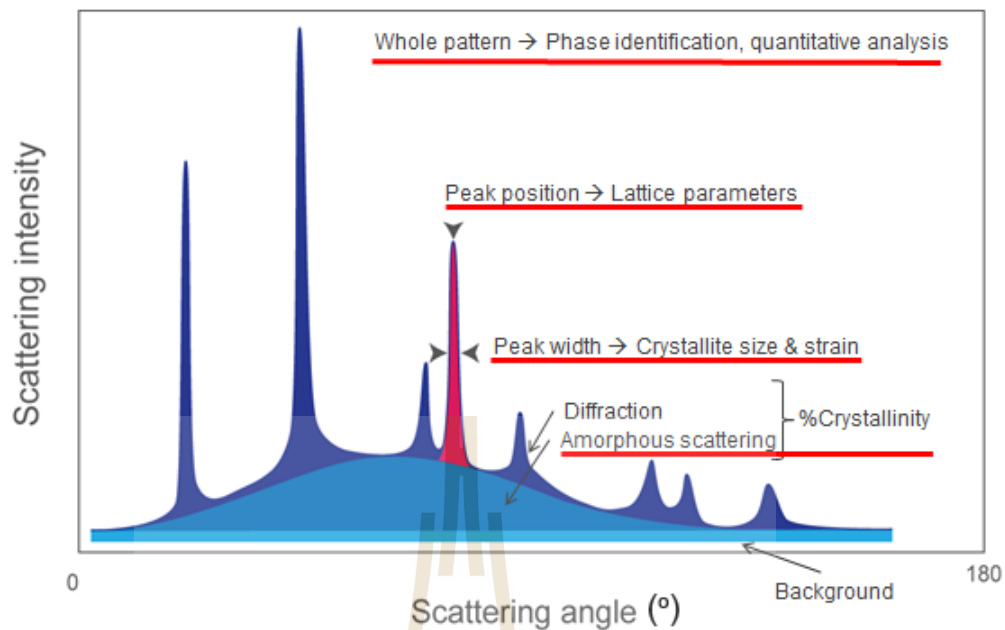
Figure 2.9 The schematic of XRD pattern and information obtainable. (https://nptel.ac.in/courses/115103030/3).

The relation of wavelength of electromagnetic radiation to the diffraction angle and the lattice spacing in a crystalline sample is Bragg's Law. when conditions satisfy Bragg's Law equation is

$$n = 2dsin\theta \tag{2.1}$$

Where θ is the scattering angle, n is a positive integer and λ is the wavelength of the incident wave.

When X-ray from source reflects on any lattice in crystal, The incident light from lattice in crystal bring about many diffraction patterns and the patterns reflect show the characterization of the structure. And the characteristic x-ray diffraction pattern lead to a typical XRD analysis.Then the X-ray diffraction patterns are the fingerprint of all crystal. And can identify the pattern of crystalline by compared with standard reference patterns.

We can calculated d -spacing and lattice parameters for the cubic from the relation between the lattice constant and d_{hkl} by used equation 2.2 and cubic system as shown in figure 2.10.

$$d_{hkl} = \frac{a}{\sqrt{h^2 + k^2 + l^2}} \tag{2.2}$$

Simple cubic   **Face-centered cubic**   **Body-centered cubic**
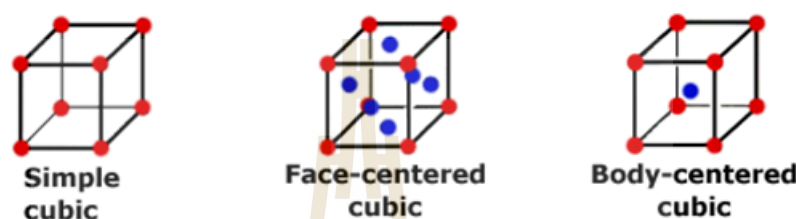
Figure 2.10 Schematic of different cubic systems.

2.2.2 Infrared Spectroscopy (IR)

We used infrared spectroscopy (IR) to determine a functional group of organic compounds. The molecules of compound absorb have a specific frequency of light in rang of IR (see in figure 2.11). The infrared region covers a spectrum wavelength rang from 0.78 mm to 1000 mm. In the context of infrared spectroscopy, wavelength is measured in "wavenumbers", which have the units cm-1and the most useful for analysis region lies from 4000 to 670 cm^{-1}.

When applied infrared radiation energies equal to the natural frequency of vibration of compound (different types of bonds absorb at different energies). The covalent bonds in molecules absorb this energy and excited to the higher energy state (from ground state). The result from the excitation takes a peak is observed. Then the infrared radiation energies from peak can indicated to the energy of functional group and the bond stretching or bending in most molecules. a sample of typical infrared absorption frequencies shown in figure 2.12.
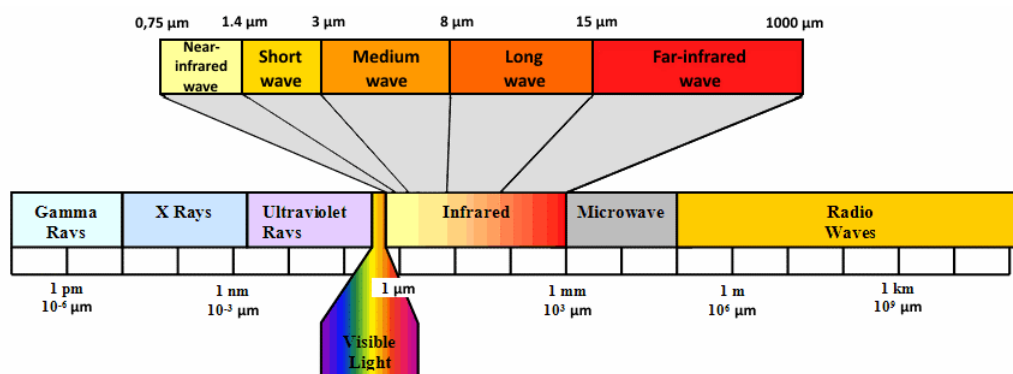
Figure 2.11 Range of infrareds.(www.pro-therm.com/images/infrared_basics)
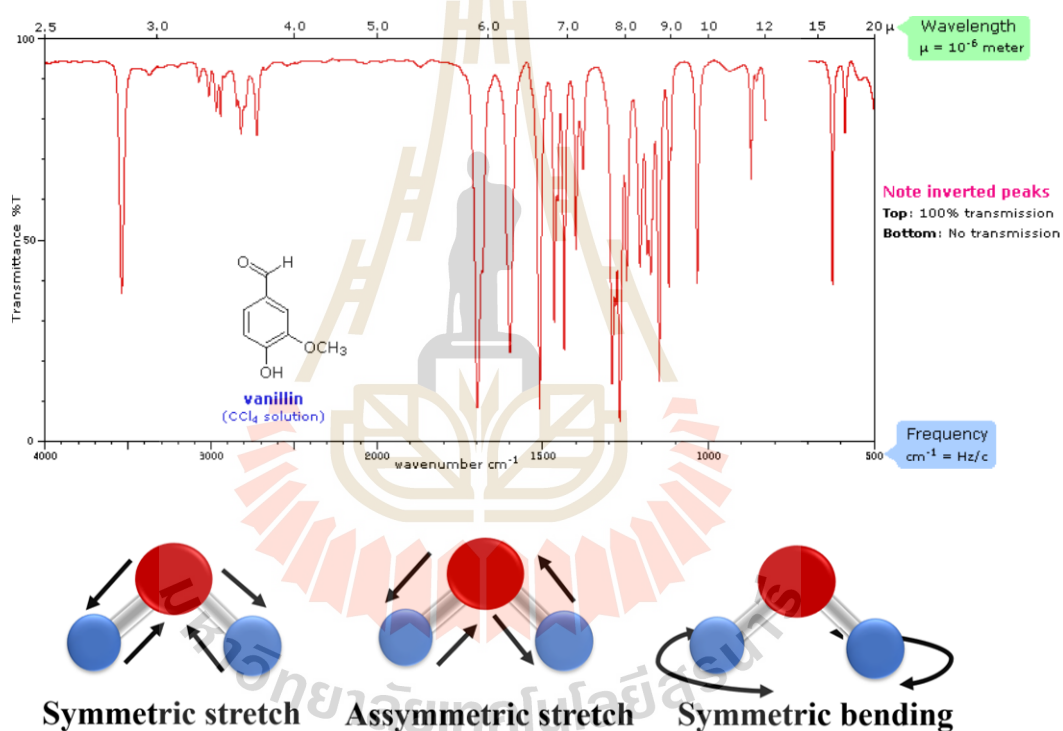
Figure 2.12 Graph of the IR spectrum and molecular vibrations.

The principle of IR instrument show in figure 2.13. The IR light from the source separate into two and passed through the reference and the sample. After light passed sample and reference and then through a detector.Finally, the light is converted into signals and displayed on the screen.
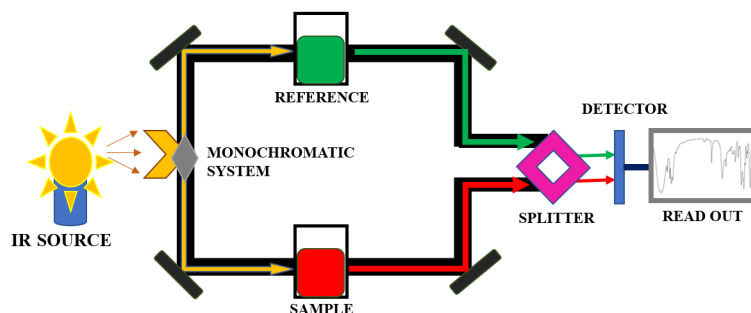
Figure 2.13 Graph of the IR spectrum and molecular vibrations.

2.2.3 Scanning electron microscopy (SEM) and energy-dispersive X-ray (EDX)

Scanning electron microscopy (SEM) is a technique for obtain high resolution images of sample by scanning over the surfaces. The high resolution image generated from black scattering of high-energy electrons emitted. Areas range of emitted approximately 1 cm to 5 microns in width. For modern SEMs can emitted in order of 2 nm. (magnification ranging from 20X to approximately 30,000X, spatial resolution of 50 to 100 nm). Scanning Electron Microscopy (SEM) have significant components of all SEMs include, electron source ("Gun"),electron lenses,sample stage,detectors for all signals of interest,display / data output devices and infrastructure requirements have power supply, vacuum system cooling system, vibration-free floor and room free of ambient magnetic and electric fields followed in figure 2.14. Electrons emission from the gun were accelerated by electric field to 20 kV. Electrons pass both of condenser and objective lenses, and then through a set of scan coils and an aperture. Electrons pass both of condenser and objective lenses, and then through a set of scan coils and an aperture. A scan is concurrently produced on a computer screen. Detects electrons emitted from the specimen, And expand and the signal will be used to create the image.
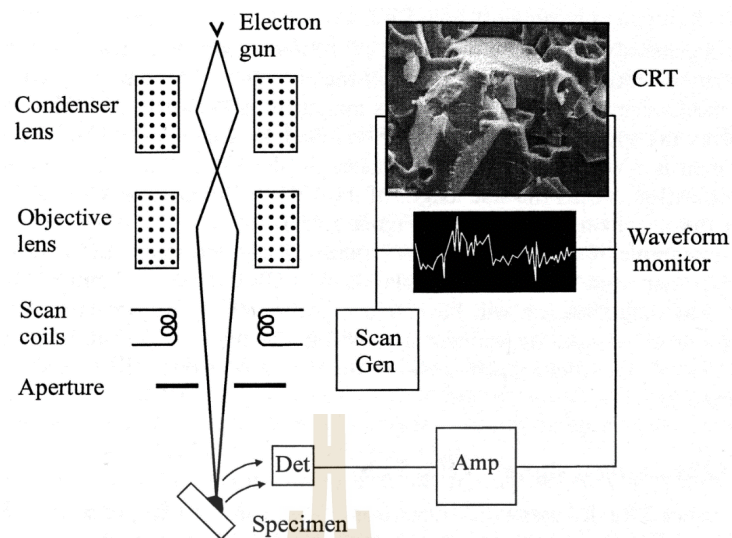
Figure 2.14 Components of the SEM.
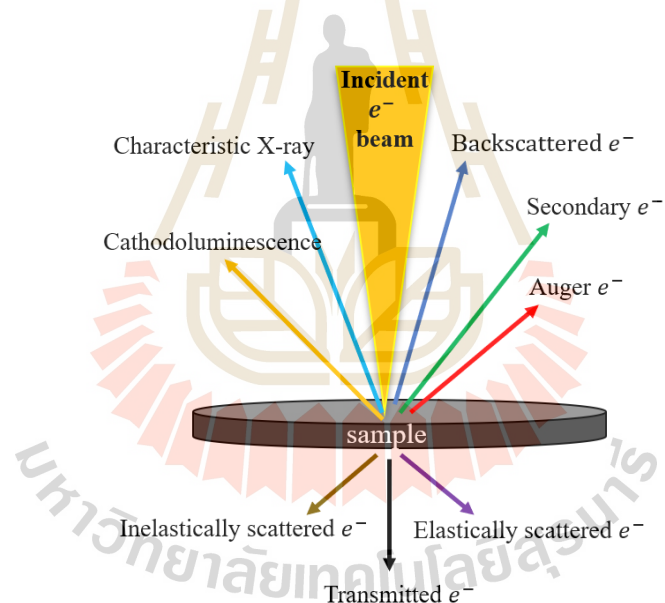
Figure 2.15 Illustration of the electron-matter interaction depicting its different-products.

Energy Dispersive X-ray Spectrometer (EDX) is an analytical technique used for the analysis of the composition or chemical properties of a sample.

2.2.4 Thermogravimetric Analysis (TGA)

Thermogravimetric Analysis (TGA) measures about weight and mass change and the rate of weight change depend on different of temperature, time and conditions. Then this measurements are used to determine the composition of materials and to predict the thermal stability. This technique can identify material loss or weight gain due to apsorption/desorption of volatiles, decomposition, oxidation and reduction.
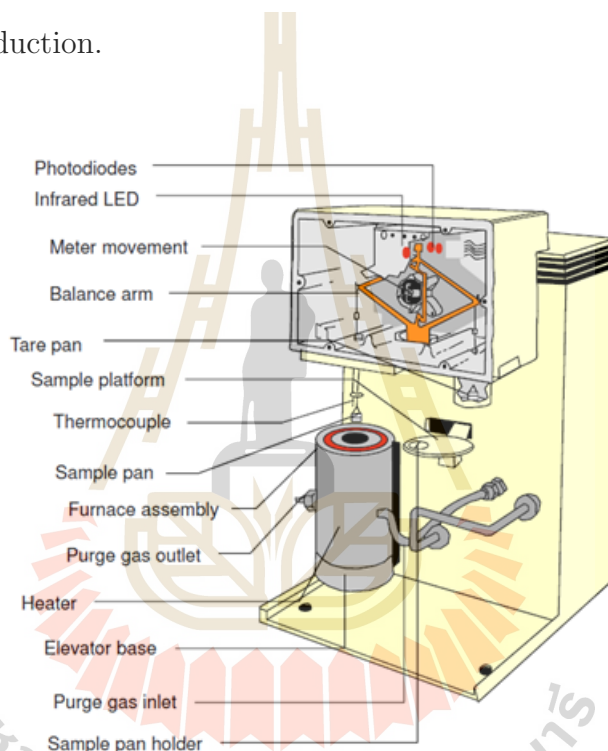
Figure 2.16 Components of the TGA.

Mechanisms of weight change in TGA. The difference weigth was result of the consist of decomposition that came from the breaking apart of chemical bonds, evaporation from the loss of volatiles with elevated temperature and reduction from interaction of sample to a reducing atmosphere(hydrogen, ammonia, etc.). And for Weight Gain consist of oxidation from interaction of the sample with an oxidizing atmosphere and absorption. All of these are kinetic processes (i.e. there is a rate at which they occur).

2.2.5 X-ray absorption spectroscopy (XAS)

X-rays are ionizing radiation,can performed at the synchrotron radiation factory, which produces intense and adjustable X-rays. Then they have energy enough to drive the core level of electrons from atoms. And each core level of each element has a different energy, so if X-ray absorption is in the form of energy, the function spectrum of any atom is similar to the X-ray absorption spectrum. The figure 2.17 show Mass Attenuation Coefficients for different element from the lower energy photons of the spectrum. The energy are almost totally absorbed by surrounding tissues, rendering K-edge imaging using iodine contrast agents. The absorption coefficient (μ) depends strongly on X-ray energy(E) and atomic number(Z), the density(r) and atomic mass(A) follow in quation 2.3. Absorption coefficient (μ) there was a sudden jump (Absorption edge) which occurs at the energy characteristics of the element.

$$\mu \approx \frac{\rho Z^4}{AE^3} \tag{2.3}$$

From the principle of X-ray radiation as above. X-ray absorption spectroscopy (XAS) is a one of technique to used X-ray radiation for determine the local geometric and/or electronic structure of material. The sample can be in a gas-phase solution or a solid.The XAS data is achieved by regulating the photon energy by using a themonochromator crystal, to a energy range of core electrons can be excited (0.1–100keV, 16–16,022 J).

An X-ray is absorbed by an atom when the energy of the X-ray is transferred to a core-level electron (K, L, or M shell) which is ejected from the atom (show in figure 2.18). The atom is left in an excited state with an empty electronic level (a core hole). Any excess energy from the X-ray is given to the ejected photoelectron. The X-ray absorption spectroscope measurement the energy dependence of the
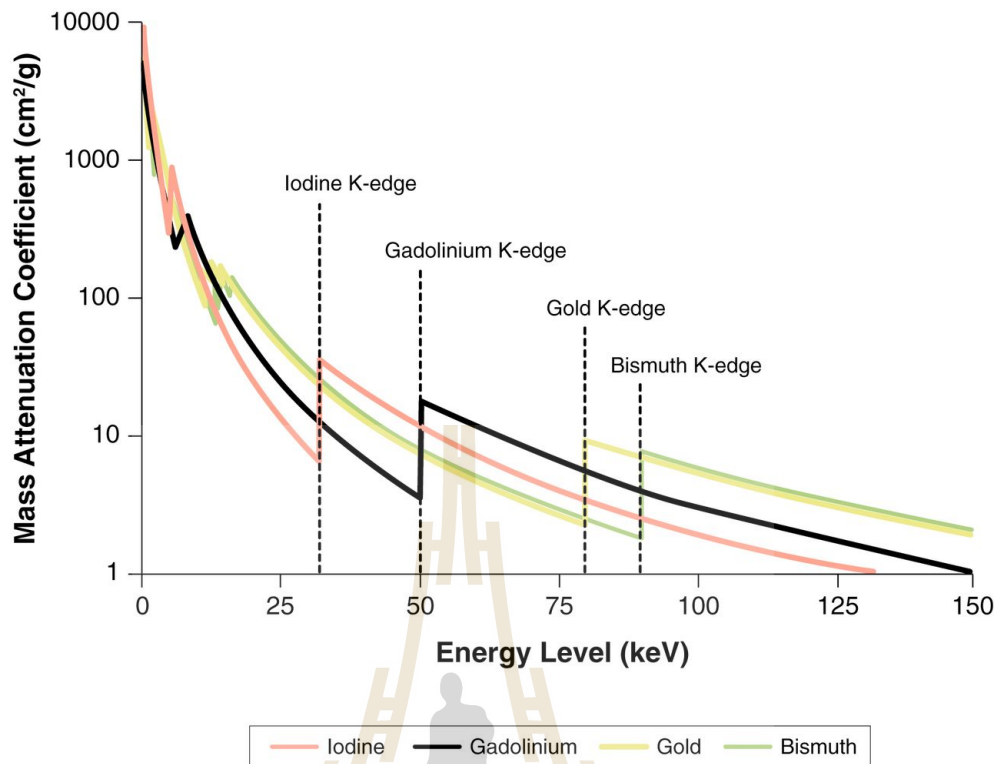
Figure 2.17 Mass Attenuation Coefficients for Iodide, Gadolinium, Gold, and Bismuth at Different Photon Energies (Danad et al., 2015).

X-ray absorption coefficient $\mu(E)$ at and above the absorption edge of selected element And $\mu(E)$ can be measured two ways:

Transmission mode: The absorption is measured directly by measuring what is transmitted through the sample:

$$I = I_0 e^{\mu(E)t} \tag{2.4}$$

$$\mu(E)t = ln(I/I_0) \tag{2.5}$$

where I_0 is the intensity of the incoming X-ray beam, I is the intensity of the beam after pass though the sample, and it is the thickness of the sample, is the definition of absorption coefficient, as shown in figure 2.19 and 2.20.
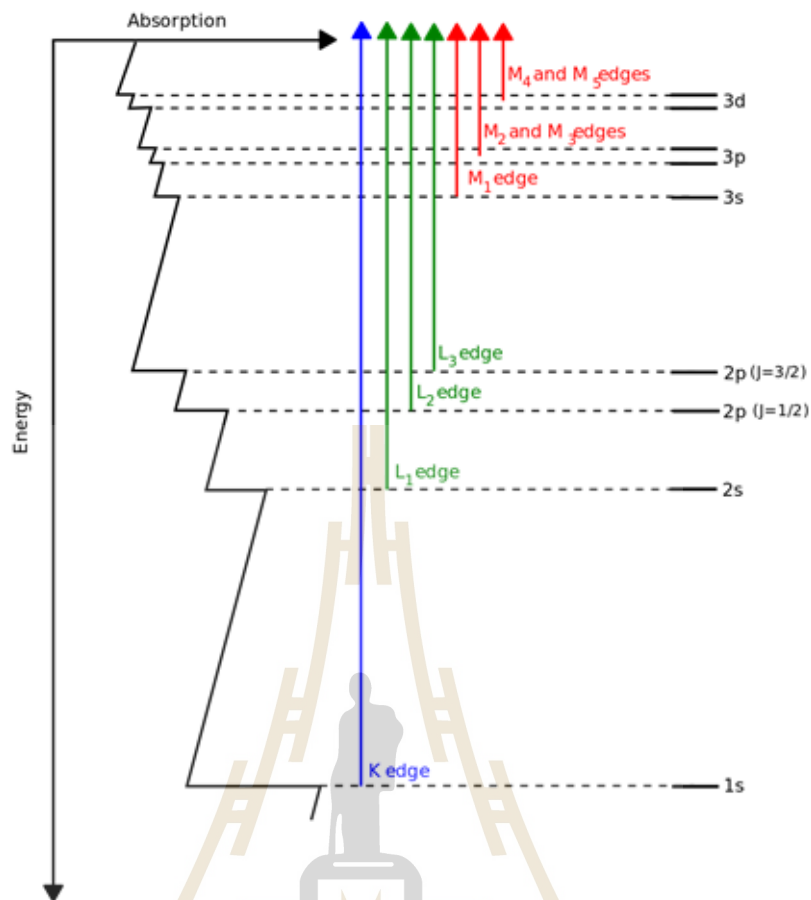
Figure 2.18 Illustrative X-ray absorption spectrum of an transition metal atom.
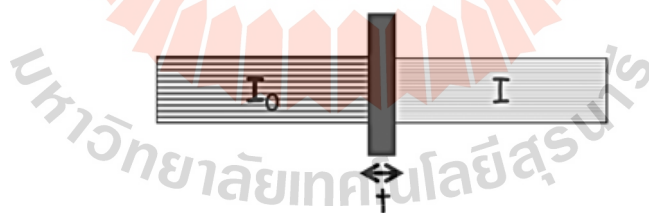
Figure 2.19 Schematic view of X-ray absorption measurement in transmission mode.

Fluorescence mode: We measured in this mode The re-filling the deep core hole is detected. Typically, the fluorescent X-ray is measured:

$$\mu(E) \sim I_F / I_0 \tag{2.6}$$
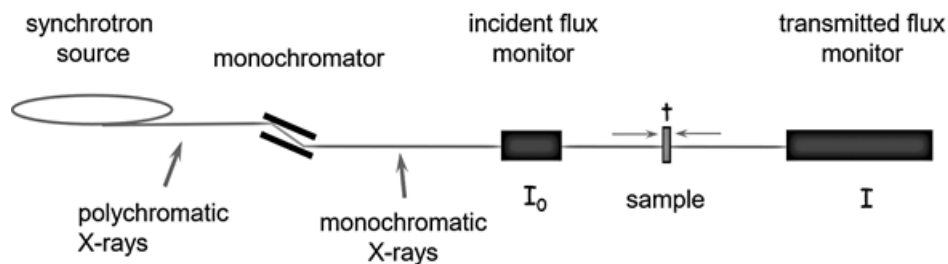
Figure 2.20 The schematic of the Absorption Coefficient μ.

DATA ANALYSIS

The spectrum signal of XAS consist of two techniques;
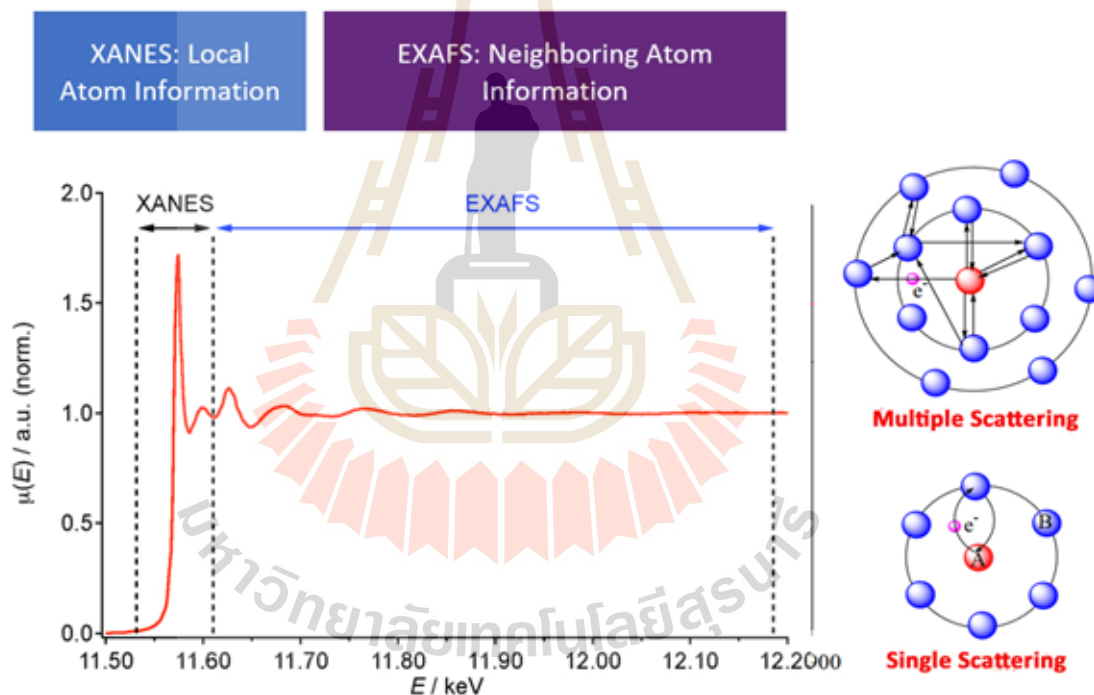
Figure 2.21 Two main regions found on a spectrum generated by XAS data.(Inc, 2018).

1. XANES (X-ray Absorption Near Edge Structure)

XANE is region of X-ray absorption spectrum within 50 eV of the absorption edge. Many edges of many elements show significant edge shifts (binding energy shifts) with oxidation state. And XANES is a strongly sensitive to the

chemistry (formal oxidation state and geometry) of the absorbing atom, it's consisted of the region of;

1.1.Pre-edge region, the transition features caused by electronic transitions to empty bound states. Transition probability controlled by dipolar selection rules. Shown the information of local geometry around absorbing atom. Dependence on oxidation state and bonding characteristics (chemical shift)

1.2.Edge region, defines ionization threshold to continuum states. The position of edge dependence on oxidation states (chemical shift), main edge shifts to higher energy with increased oxidation state. (as much as 5 eV per one-unit change).

1.3.XANES region, the transition feature dominated by multiple-scattering resonances of the photoelectrons ejected at low kinetic energy. Large scattering cross section. It's represents atomic position of neighbors or interatomic distances and bond angles. Multiple scattering dominates but ab initio calculations providing accessible insight (e.g. FEFF8)

2. EXAFS (Extended X-Ray Absorption Fine Structure)

XAS is a type of absorption spectroscopy from a core initial state with a well-defined symmetry therefore the quantum mechanical selection rules select the symmetry of the final states in the continuum which usually are mixture of multiple components. The most intense features are due to electric dipole allowed transitions (i.e. $\triangle l = \pm 1$) to unoccupied final states. For example, the most intense features of a K-edge are due to core transitions from 1s p-like final states, while the most intense features of the L_3-edge are due to 2p d-like final states. XAS methodology can be broadly divided into four experimental categories that can give complementary results to each other: metal K-edge, metal L-edge, ligand K-edge, and EXAFS.

The information of FEFF requires certain information to make its calculation.

Atomic coordinates FEFF performs its calculation on a cluster of atoms and so requires a list of Cartesian coordinates. The absorber does not need to be at (0, 0, 0).

Potential assignments Each atom is assigned a potential index along with its coordinates. This is how FEFF knows what kind of atom is at each position. Typically, each atomic species or each crystallographic position is assigned a potential.

Other parameters FEFF also needs to know which edge is to be computed (i.e., K, LIII, and so on). Another common parameter is RMAX, which limits the radial extent of the calculation. XANES calculations using FEFF8 usually require a few additional parameters.

FEEF calculation program

FEFF is an automated program for ab initio multiple scattering calculations of X-ray Absorption Fine Structure (XAFS), X-ray Absorption Near-Edge Structure (XANES) and various other spectra for clusters of atoms. The code yields scattering amplitudes and phases used in many modern XAFS analysis codes, as well as various other properties.There are steps to do as follows.

1. A FEFF input file

2. Using Atoms to prepare the FEFF input file.

3. Preparing the FEFF input file for non-crystalline materials.

4. Running FEFF

5. FEFF's output files writes several output files:

'misc.dat' General information about the potentials.

'paths.dat' Textual descriptions of all path geometries considered in the calculation.

'files.dat' A list of all path files written by FEFF.

'phase.bin' Binary file containing the data needed to compute the path files

'feffNNNN.dat' The files containing the path data. The 1st path is in 'feff0001.dat',

the 2nd in 'feff0002.dat' and so on.

FEFF8 writes several additional files containing partial electronic densities of state as well as other binary data and a file called 'feff.bin' containing all 'feffNNNN.dat' files. Finally the result from FEFF can calculated the ratio of structure in compound by ATHENA program.

```
* This feff.inp file generated by ATOMS, version 2.50
* ATOMS written by and copyright (c) Bruce Ravel, 1992-1999

* -- * -- * -- * -- * -- * -- * -- * -- * -- * -- * -- * -- * --
* -- *
*         total mu =        623.4 cm^-1, delta mu =        126.6 cm^-1
*         specific gravity = 6.849, cluster contains   67 atoms.
* -- * -- * -- * -- * -- * -- * -- * -- * -- * -- * -- * -- * --
* -- *
*         mcmaster corrections:  0.00037 ang^2 and  0.627E-06 ang^
4
* -- * -- * -- * -- * -- * -- * -- * -- * -- * -- * -- * -- * --
* -- *

TITLE    CH3NH3PbI3 tatragonal structure

EDGE     K
S02      1.0

*        pot    xsph   fms    paths genfmt ff2chi
CONTROL  1      1      1      1     1      1
PRINT    1      0      0      0     0      0

*        r_scf  [ l_scf  n_scf  ca ]
SCF      5.5         0      15     0.1

*        ixc  [ Vr  Vi ]
EXCHANGE 0      0   0

*EXAFS
*RPATH    13.75045

*        kmax  [ delta_k  delta_e ]
XANES    4.0      0.07      0.5
*        r_fms      [ l_fms ]
FMS      6.87523     0
*
RPATH    0.10000
*        emin  emax  resolution
```

Figure 2.22 The example of a FEFF input file.

```
POTENTIALS
  * ipot    z       tag
     0      17       Cl
     1      82       Pb
     2      17       Cl


ATOMS                        * this list contains 33 atoms
  *     x           y            z       ipot  tag          distance
     0.00000     0.00000     0.00000     0    Cl3          0.00000
     2.06604    -2.06604     0.00000     1    Pb2.1        2.92182
    -1.34158     1.34158     2.24086     1    Pb1.1        2.93617
    -1.34158     1.34158    -2.24086     1    Pb1.1        2.93617
    -2.68316     2.68316     0.00000     2    Cl4.1        3.79456
     3.40762    -0.72446     2.24086     2    Cl5.1        4.14224
    -3.40762    -0.72446     2.24086     2    Cl5.1        4.14224
     3.40762    -0.72446    -2.24086     2    Cl5.1        4.14224
    -3.40762    -0.72446    -2.24086     2    Cl5.1        4.14224
     0.72446     3.40762     2.24086     2    Cl6.1        4.14224
     0.72446    -3.40762     2.24086     2    Cl6.1        4.14224
     0.72446     3.40762    -2.24086     2    Cl6.1        4.14224
     0.72446    -3.40762    -2.24086     2    Cl6.1        4.14224
     0.00000     0.00000     4.48171     2    Cl3.1        4.48171
     0.00000     0.00000    -4.48171     2    Cl3.1        4.48171
     4.13207     2.68316     0.00000     2    Cl4.2        4.92680
    -2.68316    -4.13207     0.00000     2    Cl4.2        4.92680
     2.06604     4.74919     0.00000     1    Pb2.2        5.17913
    -4.74919    -2.06604     0.00000     1    Pb2.2        5.17913
     2.06604    -2.06604     4.48171     1    Pb2.3        5.35003
     2.06604    -2.06604    -4.48171     1    Pb2.3        5.35003
     4.13207    -4.13207     0.00000     2    Cl4.3        5.84364
    -2.68316     2.68316     4.48171     2    Cl4.4        5.87234
    -2.68316     2.68316    -4.48171     2    Cl4.4        5.87234
     5.47365     1.34158     2.24086     1    Pb1.2        6.06483
    -1.34158    -5.47365     2.24086     1    Pb1.2        6.06483
     5.47365     1.34158    -2.24086     1    Pb1.2        6.06483
    -1.34158    -5.47365    -2.24086     1    Pb1.2        6.06483
     4.13207     2.68316     4.48171     2    Cl4.5        6.66026
    -2.68316    -4.13207     4.48171     2    Cl4.5        6.66026
```

Figure 2.23 The example of a preparing the FEFF input.

2.2.6   X-ray photoelectron spectroscopy (XPS)

In X-ray photoelectron spectroscopy (XPS) is surface analytical techniques.
The principle of XPS is an incident X-ray photon interacts with a core electron
in a solid,gases or liquids by the photoelectric effect. The result of incident X-ray
is excited electron from the atom to surrounding material. Wherewith these core
electrons in an electronic environment is unique, depending on the species of atoms,
electrons prefer XPS provides detailed procedures for monitoring the composition

of materials.The required environment for detecting these electrons are compose of an X-ray source, a sample and an electron detector And high vacuum for increase the free path of electrons and the probability of detection,thus they are need to performed in ultra-high vacuum.

The X-ray energy from source hit on the surface and X-ray photon of energy were incidents. This energy will be absorbed by the binding energy of the atom. After the X-ray hit, The excess energy from the X-ray source used to ejected electron from the atom was detected in an analyzer. We can calculate the binding energy of electron by equation 2.7.

$$E_B = h\upsilon - E_k - \varnothing_a nalyser \tag{2.7}$$

where $\varnothing_{analyser}$ is the work function of the electron analyser, not the species in question. This means that any detected electrons provide a specific fingerprint of the atomic species in the near surface region. The chemical shifts are the slight variations of binding energy, refer to the chemical environment of atoms in the near surface region to be determined. However, due to varying x-ray absorption probabilities of different states the picture is slightly more complex. This process is shown schematically figure 2.24. A typical XPS spectrum is illustrated below. The spectrum shows a series of sharp peaks corresponding to core states of surface atoms. These peaks are accompanied by inelastic loss tail features, arising from interactions before the electrons emerge from the surface, thus, reducing their energy, This feature in itself can be used to obtain chemical depth profiles of the sample. Increasing the surface specificity of XPS can be achieved by using smaller angles of incidence. Then the XPS is the one of excellent technique for qualitative and quantitative analysis of chemical compound (L. Rosenberger).
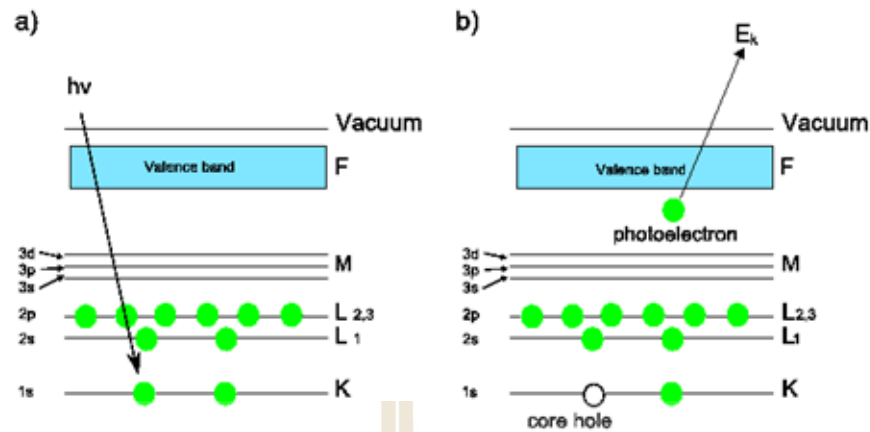
Figure 2.24 Schematic of the photoemission process in XPS. a) Incident photon energy $h\upsilon$ is absorbed by a core level electron. b) If $h\upsilon > E_k$ then the electron is emitted, and a core hole is left behind. This core hole may be filled by an electron from a higher state, causing emission of a secondary photon, or an Auger electron.

X-ray photoelectron Spectroscopy (XPS) technique used to study about elemental identification and chemical state of element, Relative composition of the constituents in the surface region. And valence band structure. We can calculate percentage of element by used equation 2.8.

$$Percentage\ for\ element\ X = \frac{\frac{I_x}{S_x T_x}}{\sum_{i=1}^{n} \frac{I_i}{S_i T_i}} x100 \qquad (2.8)$$

where n: number of regions

I: intensity

S: sensitivity factor

T: acquisition time per data point
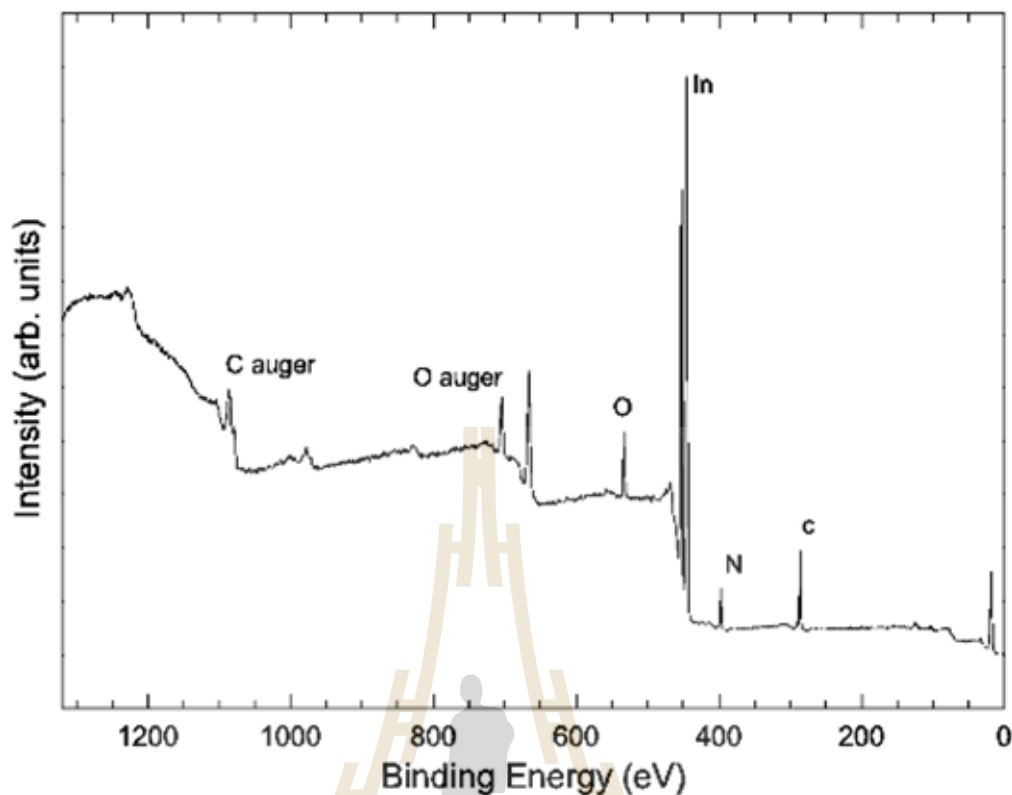
Figure 2.25 A typical XPS spectrum of an as-loaded InN sample, taken with a monochromat 1486.6 eV $Al_k - alpha$ source. Stepped structure of the background is due to inelastic processes.

2.3 CHARACTERIZATION MEASUREMENT

2.3.1 Basic characterizing of the powder of CH_3NH_3I and $CH_3NH_3PbI_{(3-x)}Cl_x$ perovskite

1. The weight loss of the $CH_3NH_3PbI_{(3-x)}Cl_x$ compound samples is studied by Thermogravimetric/Differential Thermal Analyzer (TG-DTA).

2. The size, morphology, elemental and distribution studied by Scanning electron microscopy (SEM) and Energy Dispersive X-ray (EDX).

3. The structure of the $CH_3NH_3PbI_{(3-x)}Cl_x$ compound samples is evaluated by X-ray Diffraction (XRD) and Infrared Spectroscopy (IR).

Figure 2.26 Bruker D2 PHASER.

X-ray diffraction is a standard technique for material characterization to obtain micro structural information for crystalline and non-crystalline materials. This non-destructive method could provide information's such as crystal structure, lattice parameter, crystal size, composition etc. which are useful for ceramics, metal alloys, semiconductors, polymer, nano-materials research. The X-ray diffraction is a standard technique for material characterization used by Bruker D2 PHASER. X-ray source is Ceramic Cu X-ray tube in 30 kV/ 10 mA.

Figure 2.27 FT-IR Microscope Bruker Tensor 27 with Hyperion 3000.

Bruker "Tensor 27" spectrometer with "Hyperion 3000" FT-IR microscope using a Single element MCT detector, 64*64 elements FPA detector, 20x ATR (Ge crystal) objective, 20x Ref-objective with macro-ATR-stage (600600 m FoV),GIR-objective,16x transmission and reflection objective,"KnowItAll" software package for spectrum analysis, "OPUS" software package.

2.3.2 The oxidation state of various transitions and rare earth metal ions are evaluated by X-ray Absorption Spectroscopy (XAS) and X-ray Photoelectron Spectroscopy (XPS)

1. XPS MEASUREMENTS.

XPS measurements were performed using a PHI5000 Versa probe II (ULVAC-PHI, Japan) equipped with a hemispherical electron energy analyzer at the SUT-NANOTEC-SLRI joint research facility, Synchrotron Light Research Institute (SLRI). A monochromatic Al K X-ray gun (1486.6 eV) was used as the excitation source. The XPS survey scans were collected from 0-1400 eV with pass energy 117.40 eV and energy step 1.0 eV. High resolutions XPS spectra were collected with pass energy 46.95 eV and energy step 0.05 eV for probing elements of interested. The XPS spectra were analyzed by PHI Multipak XPS software. The binding energy of all XPS spectra were calibrated with the C1s peak at 284.8 eV. The Sherly background subtraction and combinations of Gaussian-Lorentzian line shape were applied for peak deconvolution.

2. XAS MEASUREMENTS.

The XAS spectra in this thesis were obtained at the XAS facility (BL-5.2) of Siam Photon Laboratory, Synchrotron Light Research Institute, Nakhon

Ratchasima, Thailand, with the storage ring running at 1.2 GeV and beam current of 70-140 mA during the measurement. XAS measurement was performed in the transition mode using Ge (220) monochromator for I L_3-edge, Pb M_5-edge and the fluorescence mode using InSb(111) monochromator for Cl K-edge XAS spectra. And used Kapton tape and PP plastic poly bag to pack the samples for X-ray transparent.

Preparing powder sample for TM-XAS.

Figure 2.28 FT-IR Microscope Bruker Tensor 27 with Hyperion 3000.

1. Put some sample in a small agate mortar, use pestle to grind the sample into very fine powder.

2. Cut a piece of hard paper or plastic sheet to make a sample frame as shown.

3. Place a piece of thin Kapton (Polyimide) tape on the frame, sticky side up. Kapton tape should be thinner than.

4. Use sample in the mortar, weigh the right amount of the sample that equals the optimal mass, apply the sample over the sticky window area evenly and homogeneously, make sure there is no "pinhole" in the sample area. Cover the sample area with a Kapton tape.
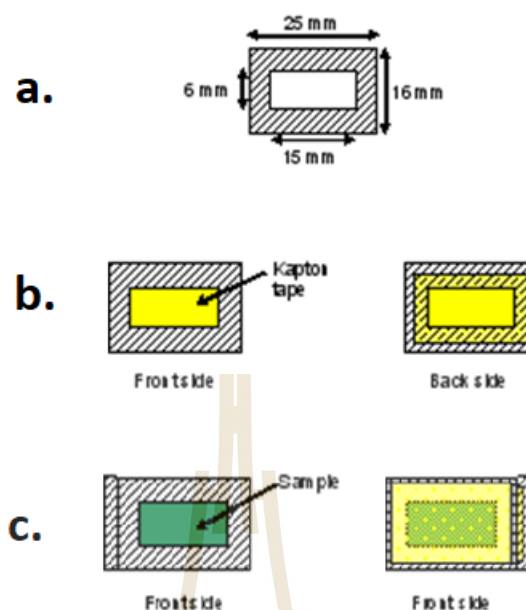
Figure 2.29 schematic to prepared powder sample for TM-XAS.

2.3.3 Population/Samplings/ Location of research

1. Materials used :

- Methylamine solution 40 wt% in H_2O, CH_3NH_2, Sigma-Aldrich

- Hydriodic acid 57 wt% distilled, 99.999% trace metals basis, HI, Aldrich

- Lead (II) chloride 99.999% trace metals basis, $PbCl_2$, Aldrich

-Acetone 99.999%, Aldrich

2. Location of research :

- Solid state chemistry Laboratory Laboratory, School of Chemistry, Institute of Science, Suranaree University of Technology, Nakhon Ratchasima, Thailand.

- The Center for Scientific and Technological Equipment, SUT.

- Synchrotron Light Research Institute (Public Organization).

3. Instrumentation :

- The Center for Scientific and Technological Equipment, SUT:

    - X-ray Diffraction (XRD)

    - Thermogravimetric/Differential Thermal Analyzer (TG-DTA)

    - Infrared Spectroscopy (IR)

    - Scanning electron microscopy (SEM) and Energy Dispersive X-ray

(EDX)

- Synchrotron Light Research Institute (Public Organization):

    - X-ray Photoelectron Spectroscopy (XPS)

    - X-ray absorption spectroscopy (XAS)
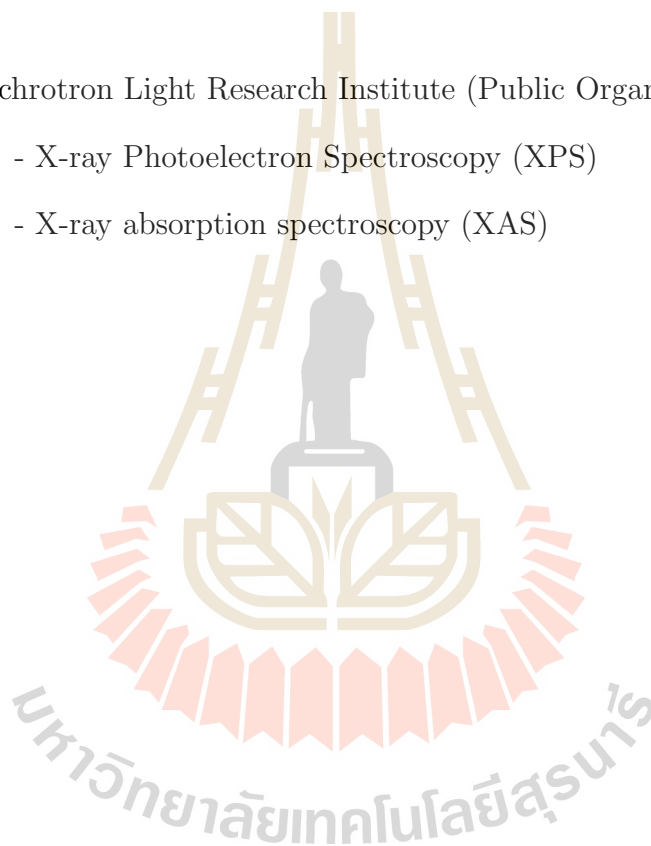
CHAPTER III

STANDARD CHARACTERIZATION

RESULTS AND DISCUSSIONS

The formation of CH_3NH_3I, $CH_3NH_3PbI_3$ and $CH_3NH_3PbI_{(3-x)}Cl_x$ was confirm by XRD, IR, XPS and XAS for investigated on the surface and interface electronic structure due to this properties can provide important of information about the physical mechanism of this kid of perovskite, It's help to improve the PCE and stability.

3.1   METHYLAMMONIUM IODIDE

Methylammonium iodide are organic group as a component of perovskite crystalline solar cell. And the iodide is the most commonly used. In this research we changed a solvent for reduced I_2 from Sero-gel in Sol-gel method. And we found a new solvent for refuses I_2 can decreased times to prepared methylammonium iodide powder 4 times from the former solvent. Then first of all, we use X-ray diffraction (XRD) for investigated crystalline of CH_3NH_3I powder, The XRD measurement was performed in ambient condition. The X-ray diffraction patterns were obtained using a Bruker instrument Cu K beam (λ= 1.54 $\mathring{A}$). As shown in the XRD pattern in figure 3.1 shown the pattern of CH_3NH_3I (MAI) dissolved in diethyl ether after that precipitation in N, N-dimethylformamide (DMF), CH_3NH_3I washed by acetone and dry in Ar (AC_Ar) and CH_3NH_3I washed by acetone (AC_Air). The typically indexed the peaks of a orthorhombic lattice in all
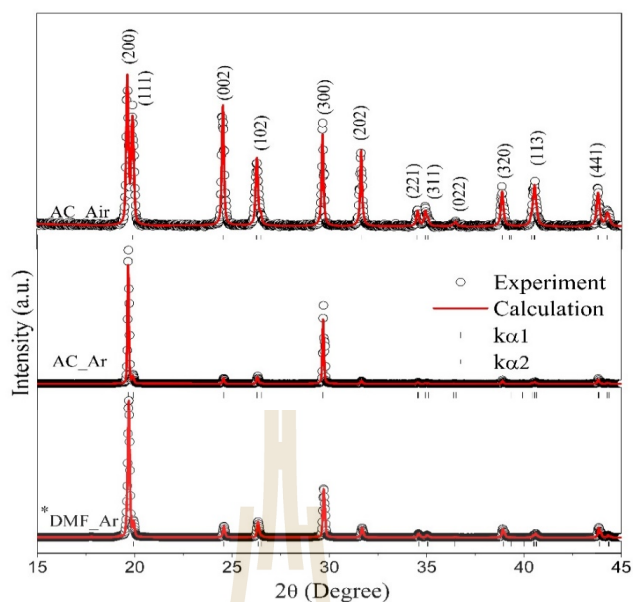
Figure 3.1 X-ray diffraction pattern of CH_3NH_3I powder in different condition and the most obvious pattern of orthorhombic lattice is clearly in CH_3NH_3I washed by acetone (AC_Air).

of samples. The both of CH_3NH_3I (MAI) dissolved in diethyl ether after that precipitation in N,N-dimethylformamide (DMF) and washed by acetone and dry in Ar (Ar) have a similar of intensity of peak. We investigated organic group of CH_3NH_3I from the figure 3.2 shown the Infrared absorption data functional groups of CH_3NH_3I washed by acetone and dry in Ar (AC_Ar) and CH_3NH_3I washed by acetone (AC_Air). The absorption cited are associated with stretching and bending vibrations of organic group in CH_3NH_3I. The peaks in IR spectrum in the region 1400, 1480, 1700 cm^{-1} and 2700,2950,3100 cm^{-1} are sharp, strong peak of C-H bending and stretching, in the region 920, 1250 cm^{-1} are the sharp, strong peak of C-N stretching, in the region 1550 cm^{-1} is the medium, broad peak of N-H bending. And in the region 3500 cm^{-1} is weak, broad peak of O-H stretching absorption of alcohol. But O-H stretching just found in CH_3NH_3I washed by acetone (AC_Air).it came from H_2O due to MAI are sensitive of moisture and in this

position to observe the force vibration between O-H weaker than N-H. then this peak is weak and broad more than the vibration of peak of N-H. and in a long time when we keep the MAI in dry cabinet. we found the CH_3NH_3I washed by acetone and dry in air, decompose quickly than CH_3NH_3I washed by acetone and dry in 60°C Ar.
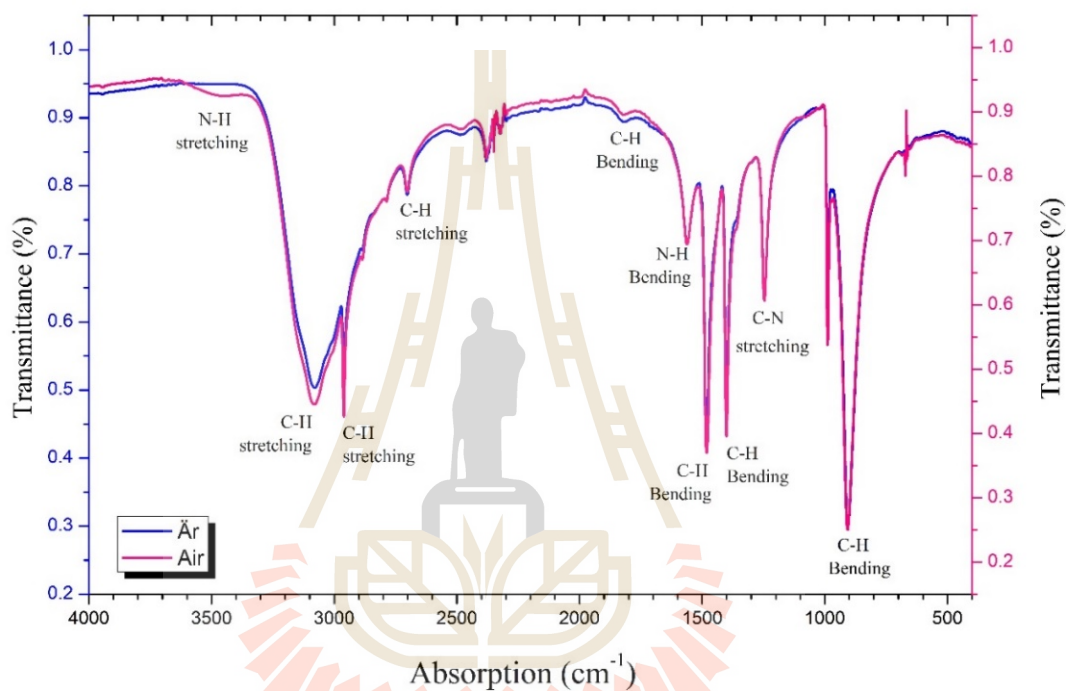
Figure 3.2 The Infrared absorption data functional groups of CH_3NH_3I washed by acetone and dry in Ar (AC_Ar) and CH_3NH_3I washed by acetone (AC_Air).

The data of XPS in figure 3.3 shows spectra from a PHI5000 Versa probe II (ULVAC-PHI, Japan) equipped with a hemispherical electron energy analyzer, the excitation source used by a monochromatic Al Kα X-ray gun (1486.6 eV). The core level of spectra in C1s to consist of two peaks position follow at table 3.1 and XPS FWHMs at table 3.2. The core level is position 284.93, ~286.43 and ~285, ~286.55 in MAI_(AC_Ar) and MAI_(AC_Air), respectively. The core level is position ~284.93 eV and ~285 referred to C-H and C-C bonding. And the core level

46
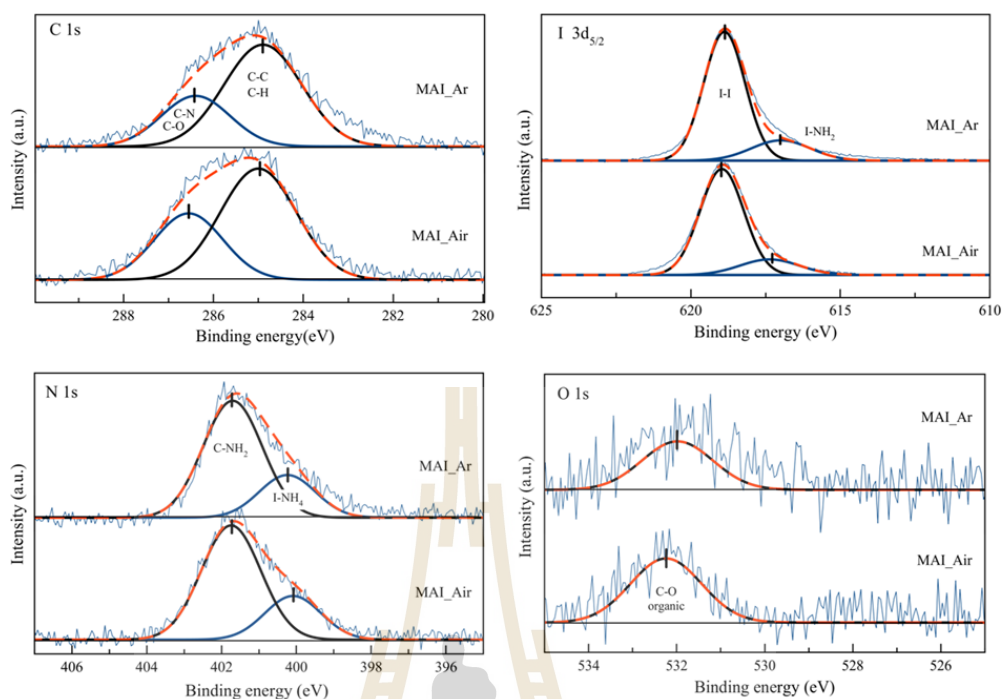
Figure 3.3 The data of XPS of CH_3NH_3I powder.

Table 3.1 XPS core level positions, elemental bonding and percent of element in compound of CH_3NH_3I .

Samples	Core level center (eV)						
	C 1s		I 3d5		N 1s		O 1s
	1	2	1	2	1	2	1
MAI_(AC_Ar)	286.43	284.93	618.88	616.99	401.70	400.24	531.98
Bonding	C-C	C-N	I-I	I-NH$_4$	I-NH$_4$	C-NH$_4$	C-O
Percent of elements	54.31		21.16		22.55		1.97
MAI_(AC_Air)	286.55	285	619	617.36	401.74	400.10	532.24
Bonding	C-C	C-N	I-I	I-NH$_4$	I-NH$_4$	C-NH$_4$	C-O
Percent of elements	53.67		20.16		22.95		3.22

is position ∼286.43 eV and ∼286.55 eV referred to C-N and C-O bonding. They are overlays due to energy bonding of element is very close (Li et al.,2015).

Table 3.2 XPS FWHMs of element in compound of CH_3NH_3I in different condition to dry.

Samples	Core level center (eV)						
	C 1s		I 3d5		N 1s		O 1s
	1	2	1	2	1	2	1
MAI_(AC_Ar)	1.8	2.04	2	2.33	1.87	1.77	1.89
MAI_(AC_Air)	1.8	2	2	2.33	1.87	1.77	1.9

For the evident of XPS data, the CH_3NH_3I washed by acetone and dry in Ar (AC_Ar) we found the peak of carbon for C-H and C-C bonding has a high ratio than CH_3NH_3I washed by acetone after that dry in air (AC_Air). And the CH_3NH_3I washed by acetone and dry in Air (AC_Air) the peak of C-N and C-O bonding has a high ratio than CH_3NH_3I washed by acetone after that dry in Ar (AC_Ar). That can refer to the compound of CH_3NH_3I washed by acetone and dry in Air (AC_Air) have a contaminate with Oxygen or moisture than CH_3NH_3I washed by acetone and dry in Ar (AC_Ar). And the ratio of oxygen in AC_Air is more than AC_Ar then CH_3NH_3I (AC_Ar) is lower contaminate than CH_3NH_3I dry in air (AC_Air). The data analysis clearly about the percentage for elemental of CH_3NH_3I can calculated follow equation below and shown the percentage of element in table 3.1.

The XANES analysis of MAI from the figure 3.4 I L_3-edge spectral feature are sensitive to the local of I. The spectral feature of MAI wash by acetone and dry in air, dry in Ar and recrystallized in DMF shown the local geometry, charge state and orbital occupancy are same. And we used ATHENA program to fitting
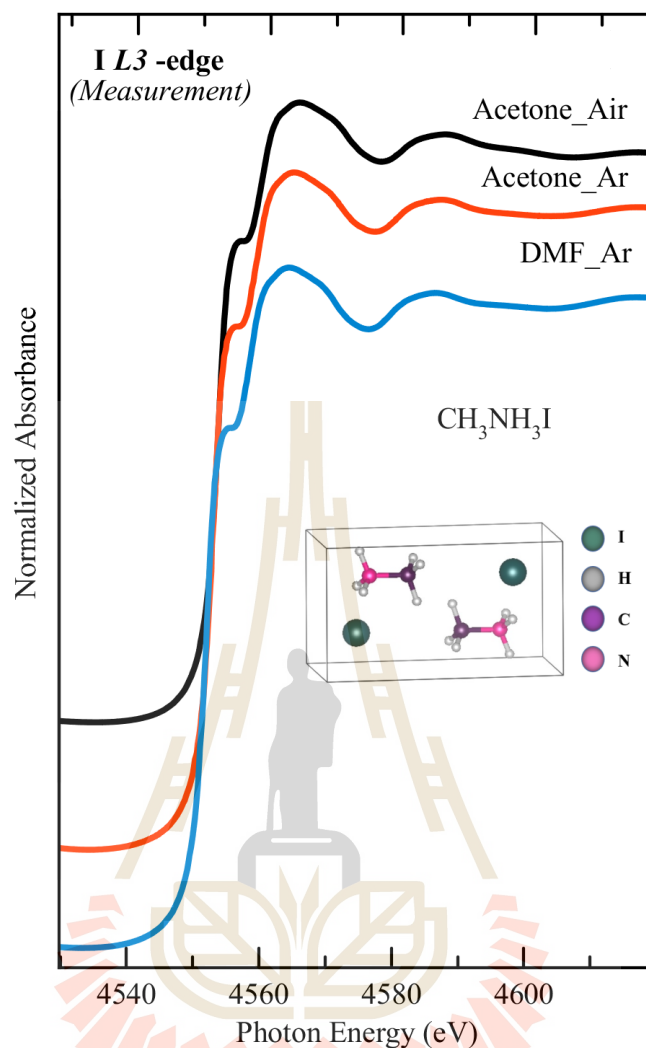
Figure 3.4 Normalized L_3 edge XANES spectra of Iodide for MAI wash by acetone and dry in air, dry in Ar and recrystallized in DMF.

combination standard (DMF) spectra to sample spectra. We found MAI wash by acetone and dry in air (Ace_Air) have constrain the variable weight 0.814 like a standard and MAI wash by acetone and dry in Ar (Ace_Ar) have constrain the variable weight 0.186 like a standard. Then We choose CH_3NH_3I (MAI), It reduced I_2 by Acetone and dry in Ar replace to MAI in DMF for as the precursor of $CH_3NH_3PbI_3$ because they are stable in H_2O and lower contamination than MAI wash by acetone and dry in air.

3.2 METHYLAMMONIUM LEAD IODIDES
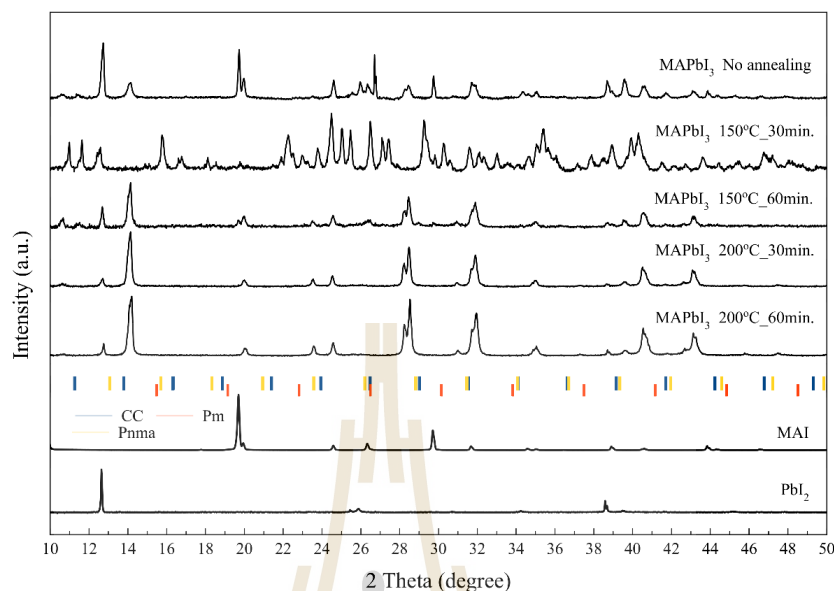
Figure 3.5 X-ray diffraction pattern of $CH_3NH_3PbI_3$ powder.

The first of all we characterized $CH_3NH_3PbI_3$ powder by used XRD.And from the figure 3.5 shown the pattern of X-ray diffraction of perovskite powder made from a 1:1 molar mixture of PbI_2 and MAI in acetone and dry in Ar. Shown the typical peaks at 14.10°, 23.47°, 28.42°, 30.89° correspond to (110), (211), (220), (213) of the tetragonal phase perovskite, respectively. And figure 3.12 shown the spectral feature of I L_3-edge spectra feature are sensitive to the local of I. The spectral feature of all sample of perovskite is same about oxidation number and shape of molecules. Then the CH_3NH_3I wash by acetone and dry in Ar. Can used to the precursor for synthesis perovskite similar to CH_3NH_3I dissolved in diethyl ether after that precipitation in N, N-dimethylformamide and dry in Ar, which takes longer 4times in a new solution for wash.

We calculated particles size of the $CH_3NH_3PbI_3$ powder surface on annealing at 200°C in 30 minutes and 60 minutes by Image J program. In figure 3.7 we found the particle size of $CH_3NH_3PbI_3$ on annealing at 200°C in 30 minutes has
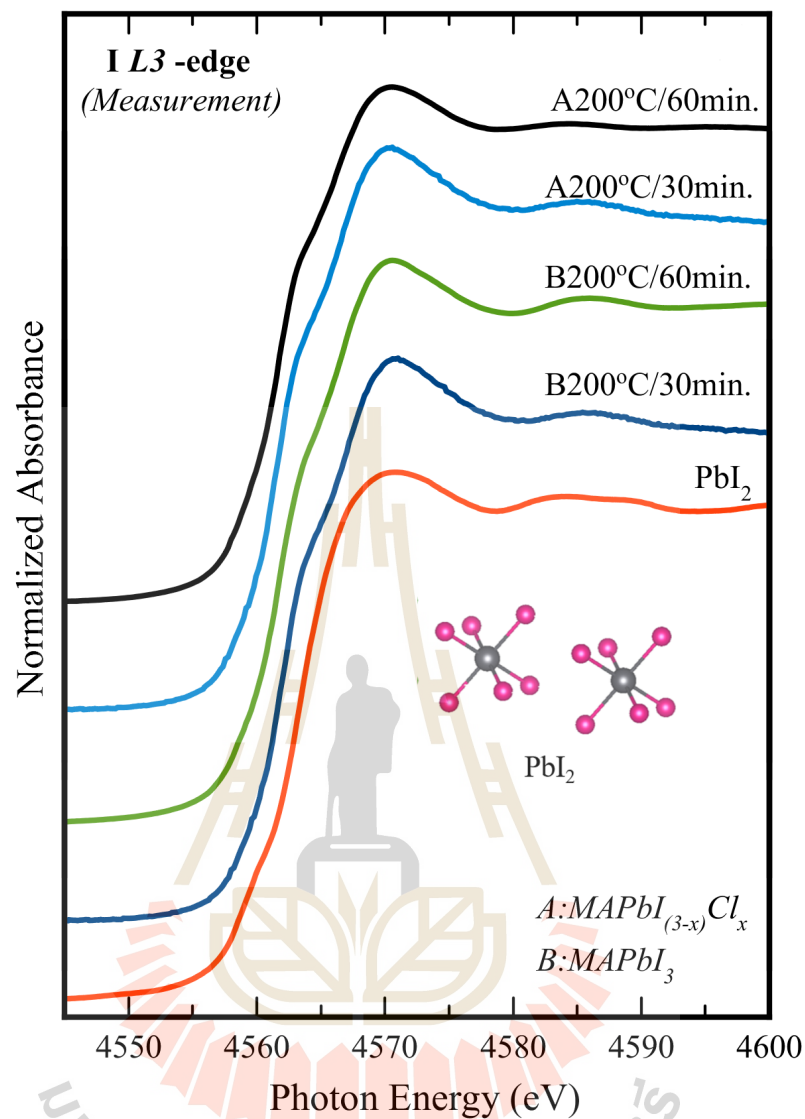
Figure 3.6 Normalized L$_3$-edge XANES spectra of Iodide for CH$_3$NH$_3$PbI$_3$ powder compared with PbI$_2$ (precursor).

52.02 nm and CH$_3$NH$_3$PbI$_3$ on annealing at 200°C in 60 minutes has 47.80 nm. And on annealing in 60 minutes with similar size more than 30 minutes because more time is available for nucleation and growth of the new recrystallized grains.

The MAI precursors from different solvents were used to synthesis hybrid perovskite CH$_3$NH$_3$PbI$_3$ powders by solid state method with varying conditions. The characterizations by X-ray Diffraction (XRD), Infrared Spectroscopy (IR), X-
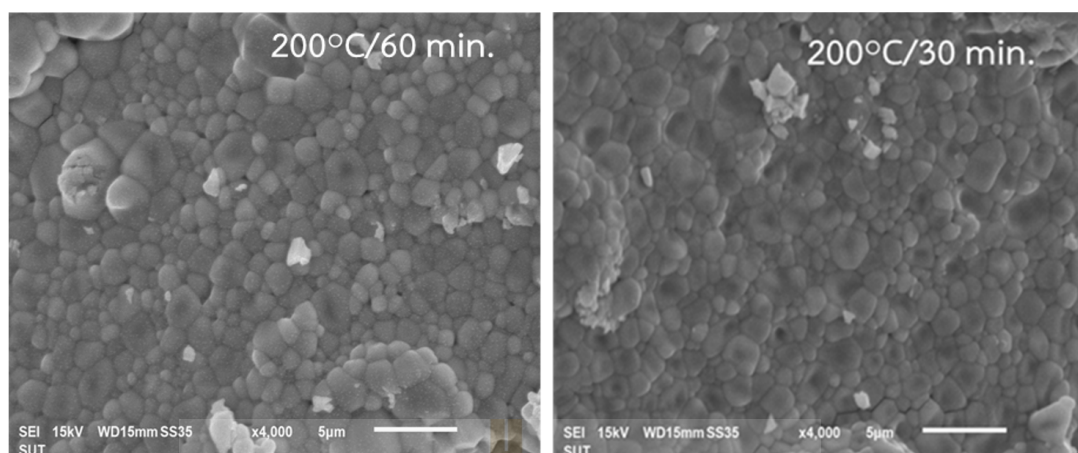
Figure 3.7 SEM image of the $CH_3NH_3PbI_3$ powder surface on annealing at 200°C in 30 minutes and 60 minutes.

ray photoelectron spectroscopy (XPS) and X-ray absorption spectroscopy (XAS) shown that the characteristic quality of hybrid perovskite $CH_3NH_3PbI_3$ powders from acetone and DMF are comparable thus confirm the effective of the new preparation route. From the result as I previously mentioned of CH_3NH_3I power precursors from different solvents were used to synthesis hybrid perovskite $CH_3NH_3PbI_3$.

3.3   METHYLAMMONIUM LEAD IODIDE CHLORIDE
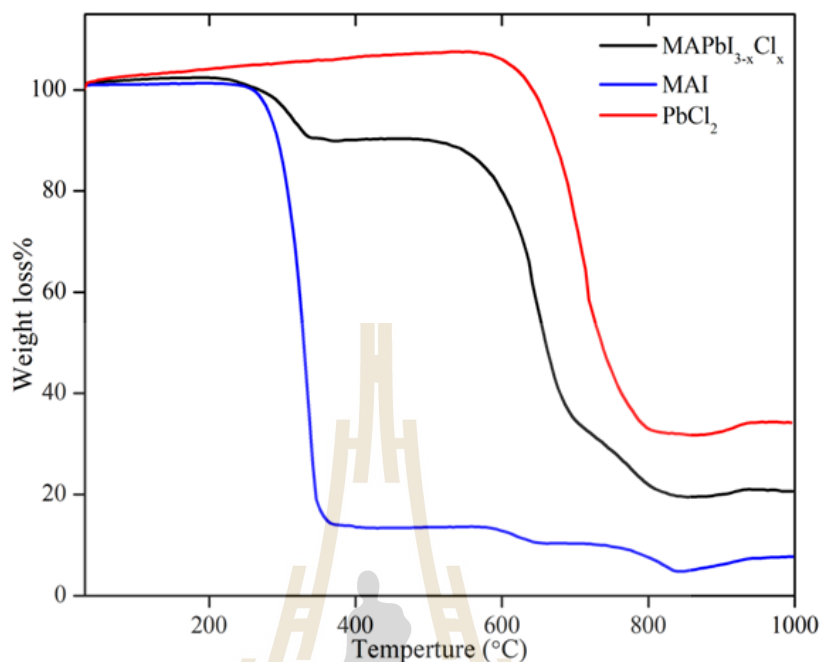
Figure 3.8 TGA curves for CH_3NH_3I, $PbCl_2$ and $CH_3NH_3PbI_{(3-x)}Cl_x$ powders.

Thermogravimetry analysis (TGA) is usually used in order to determine the suitable temperature to be used for annealing $CH_3NH_3PbI_{(3-x)}Cl_x$ powders. From the figure 3.8 when we increase temperature around 250°C organic group (MAI) are loss form 100%weight to 18 %weight, We should not annealing at 250°C the because MAI will be decomposed. Then, we choose rang of temperature to annealing form 100 to 250°C for my experiment.

From the figure 3.9 the pattern of X-ray diffraction shows pattern of XRD from precursor in (MAI: $PbCl_2$) difference molar of ratio. we found the structure of perovskite is clearly in molar ratio of precursor 1:1. And in precursor MAI: $PbCl_2$ molar ratio of 2:1 and 3:1 have many of phase so it's impurities more than 1:1. Then we focus only molar ratio of precursor 1:1 for study structure and properties of perovskite.
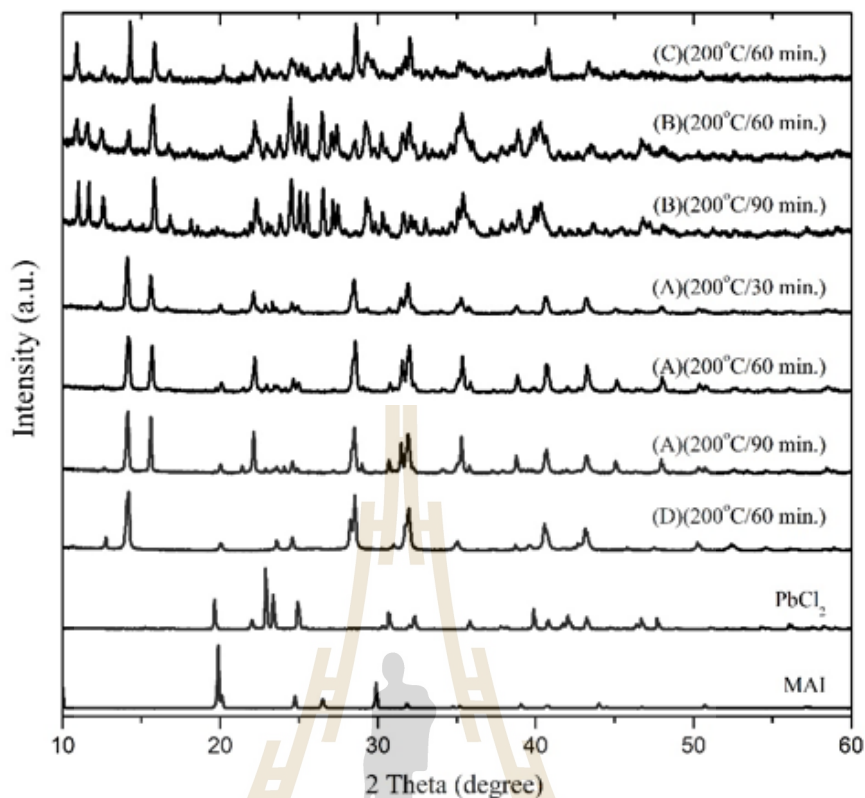
Figure 3.9 Pattern of XRD from precursor (MAI: PbCl$_2$) in difference molar of ratio 1:1(A), 2:1(B), 3:1(C) and MAPbI$_3$ (D).

From the figure 3.10 the pattern of X-ray diffraction shows pattern of XRD from precursor in (MAI: PbCl$_2$) molar of ratio 1:1 in different temperature and time we found the structure of perovskite begin to form a structure at 100°C but it's not all of powder form to perovskite structure and after we annealing at 150°C in 90 min. the structure of perovskite is clearer but has a peak intensity of CH$_3$NH$_3$Cl ; MACl higher than phase of perovskite then the crystalline of MACl more than crystalline of perovskite . At 200°C in 30, 60 and 90 min. the intensity of perovskite phase is clearly and higher than MACl. Then we will focus on this point to annealing due to the crystalline phases are mixture about perovskite phase and CH$_3$NH$_3$Cl obvious. The symbols $*$, $+$ and $\#$ denote the peaks of CH$_3$NH$_3$PbI$_{(3-x)}$Cl$_x$ perovskite, PbI$_2$ and CH$_3$NH$_3$Cl, respectively; the unlabeled
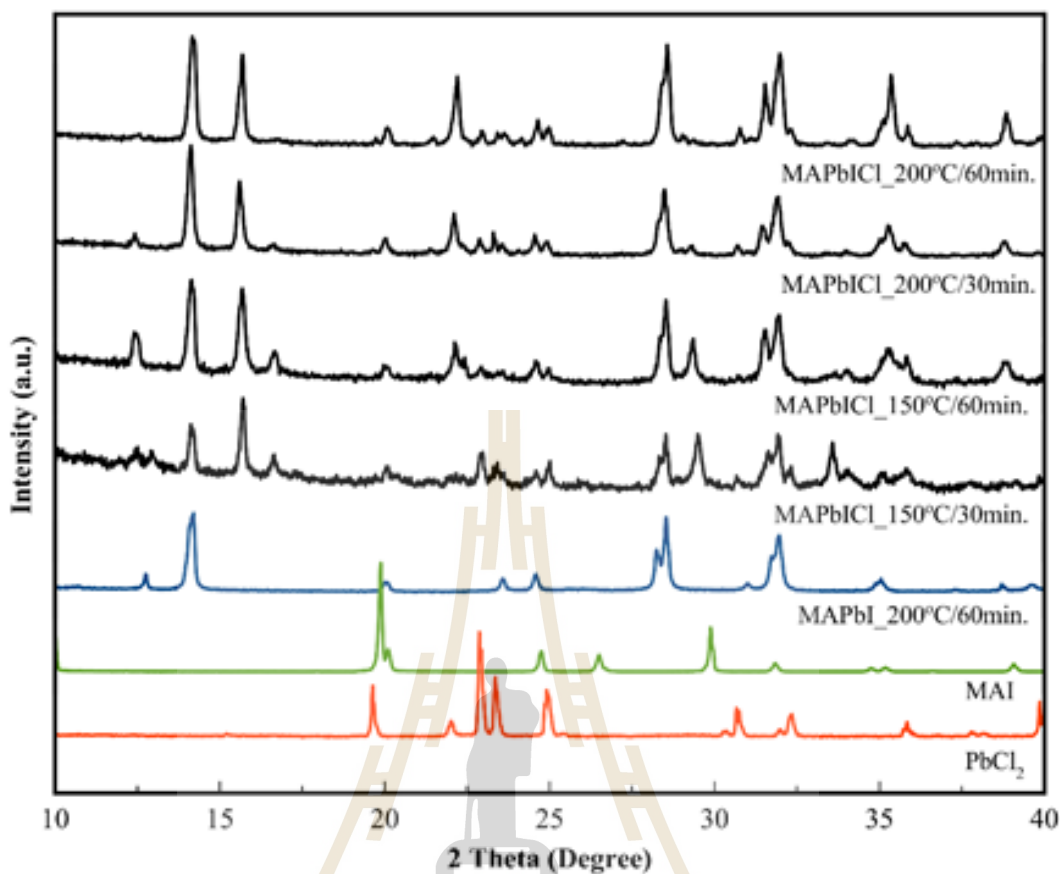
Figure 3.10 The pattern of XRD from precursor molar of ratio 1:1 (MAI: $PbCl_2$) in different temperatures and times compared with $CH_3NH_3PbI_3$.

peaks are attributed to the intermediate phase.

Form the figure 3.12 shown the peak position of peak perovskite structure (peak in left-hand side) shift to higher theta and CH_3NH_3Cl (peak in right-hand side) has a shape peak, when we increase time to annealing. Shifting of peak is can refer to Cl replace to I in structure of perovskite. But the Cl anion is a different size with I anion then Cl anion is very little possibility that to replace to I anion. We will calculate the possibility of Cl replacement in I by use XAS technique for characterized the local structure of Cl atom and use FEFF program to compare ratio of $CH_3NH_3PbI_{(3-x)}Cl_x$ perovskite and CH_3NH_3Cl in this material.
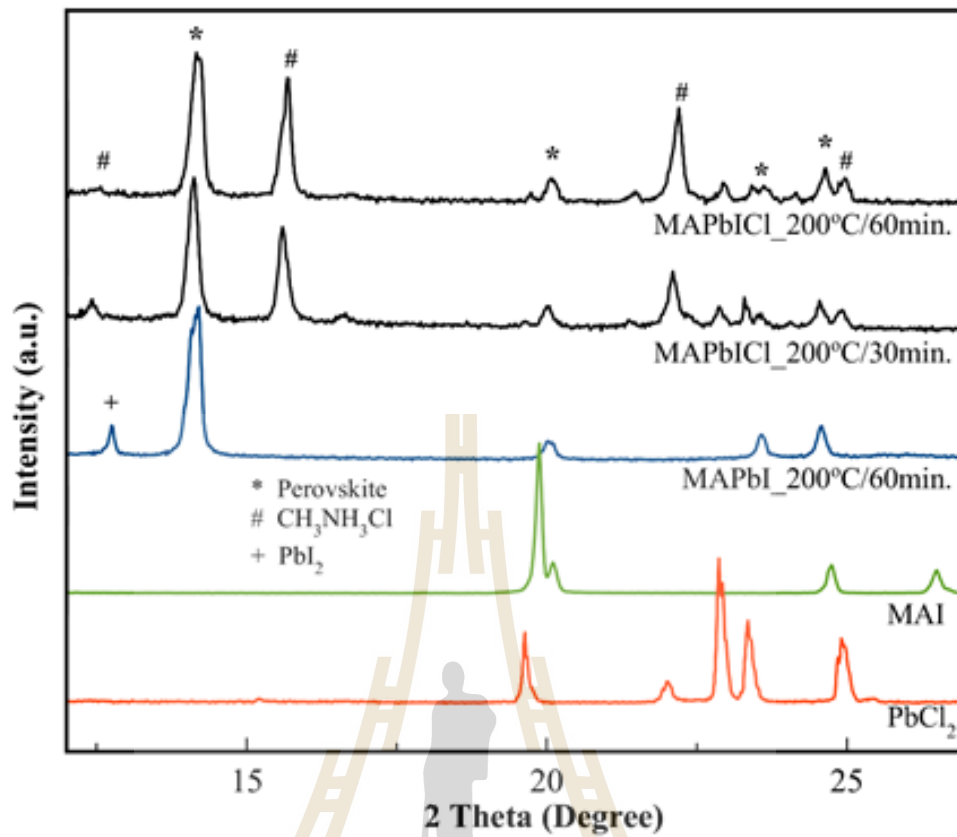
Figure 3.11 The XRD patterns for the molar ratio of precursor MAI and $PbCl_2$ is 1:1(A) annealed for 30 and 60 mins at 200°C compared with $CH_3NH_3PbI_3$.

The possible chemical reactions involved in the perovskite formation process from precursor (MAI: $PbCl_2$) molar of ratio 3:1 (1) may involve several intermediate steps. Firstly, since the amount of CH_3NH_3I in molar is 3 times that Reaction (1):

$$PbCl_2 + 3CH_3NH_3I \rightarrow CH_3NH_3PbI_3 + 2CH_3NH_3Cl(g) \uparrow \qquad (3.1)$$

Reaction (2):

$$PbCl_2 + 3CH_3NH_3I \rightarrow PbI_2 + CH_3NH_3I + 2CH_3NH_3Cl \qquad (3.2)$$

$$PbI_2 + CH_3NH_3I + 2CH_3NH_3Cl \rightarrow CH_3NH_3PbI_3 + 2CH_3NH_3Cl(g) \uparrow \quad (3.3)$$
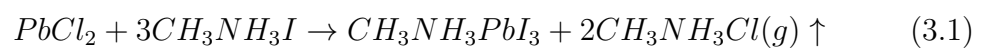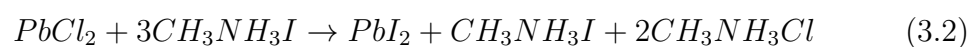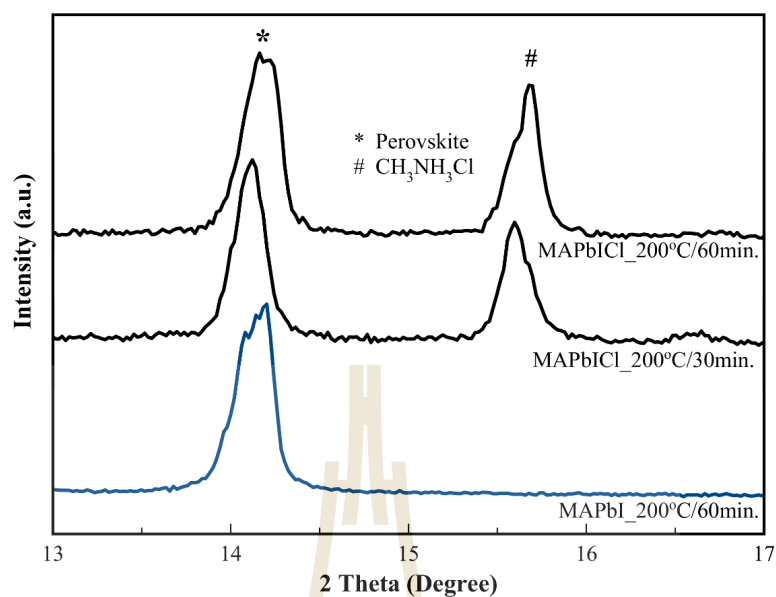
Figure 3.12 The pattern of XRD from precursor molar of ratio 1:1 (MAI: PbCl$_2$) in different temperatures and times compared with CH$_3$NH$_3$PbI$_3$.The symbols $*$ and # denote the peaks of CH$_3$NH$_3$PbI$_{(3-x)}$Cl$_x$ perovskite, PbI$_2$ and CH$_3$NH$_3$Cl, respectively
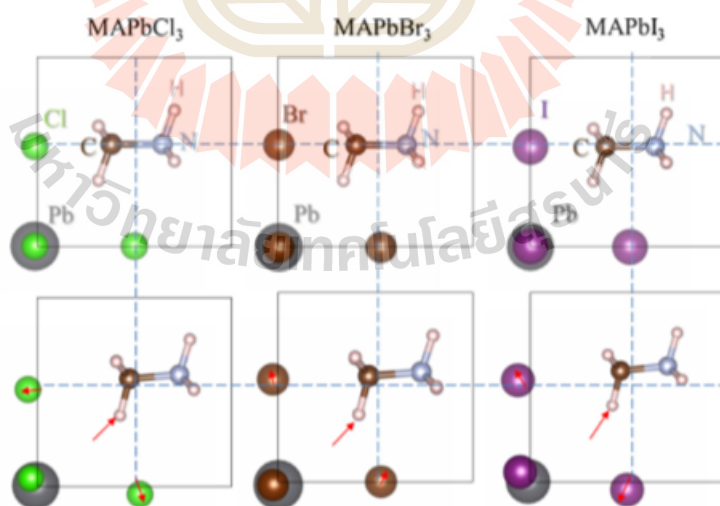
Figure 3.13 Structural optimization of MAPbX$_3$.

From reaction in equation (3.3) CH_3NH_3I react with PbI_2 or $PbCl_2$ to form the dark brown $CH_3NH_3PbI_3$ and $CH_3NH_3PbI_{(3-x)}Cl_x$ perovskite respectively. And have the phase of CH_3NH_3Cl in $CH_3NH_3PbI_{(3-x)}Cl_x$ perovskite powder, the excess CH_3NH_3Cl escapes from the film through either sublimation or decomposition into other gaseous Cl-containing mixtures (Pan et al.,2016).
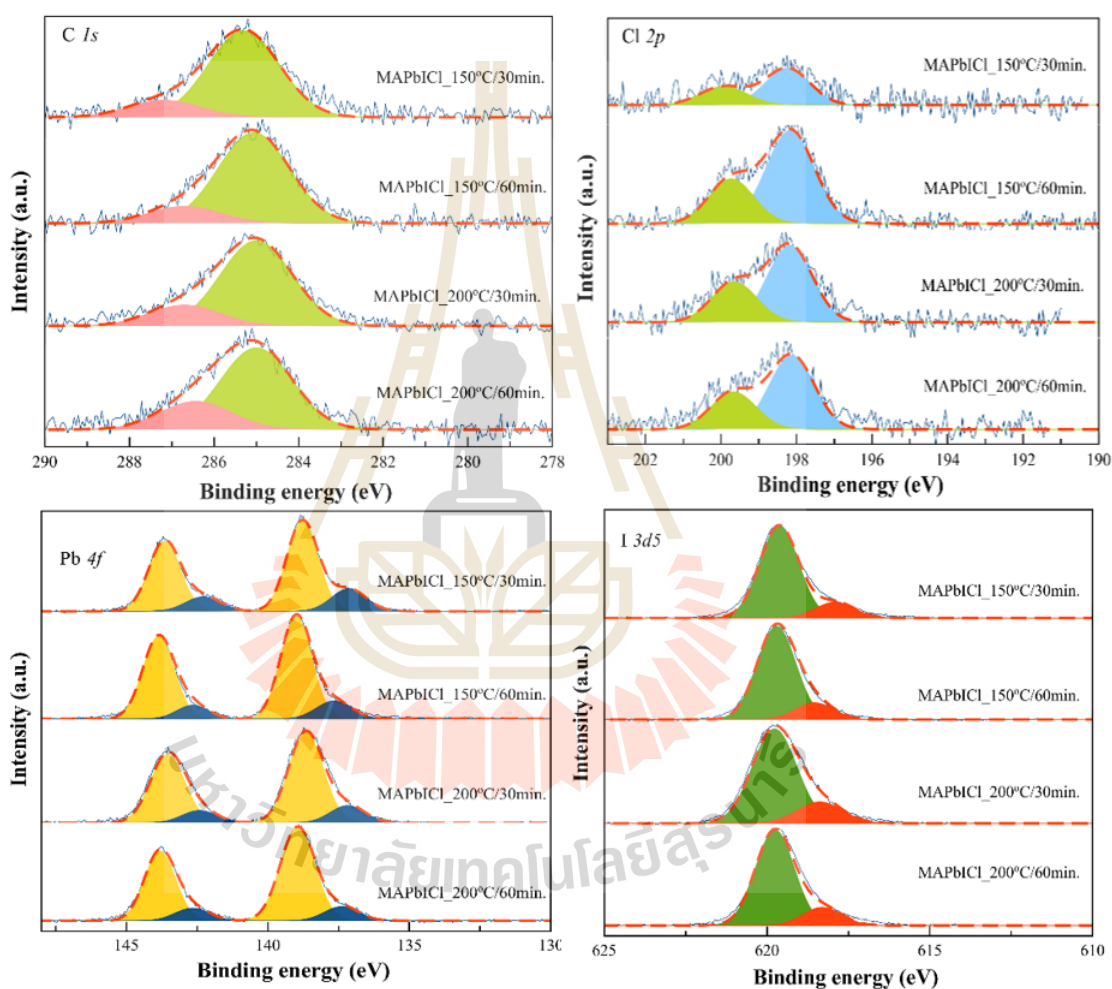
Figure 3.14 XPS core level peak of $CH_3NH_3PbI_{(3-x)}Cl_x$ powder of the Gaussian fitting and background subtraction.

The data of XPS in figure 3.14 shows spectra from a PHI5000 Versa probe II (ULVAC-PHI, Japan) equipped with a hemispherical electron energy analyzer, the excitation source used by a monochromatic Al $K\alpha$ X-ray gun (1486.6 eV).

Table 3.3 Percent of elements from XPS of $CH_3NH_3PbI_{(3-x)}Cl_x$ annealing at 150°C and 200°C.

Samples	Percent of elements			
	C	Cl	I	Pb
150°C/30 min.	50.37	4.52	28.02	17.09
150°C/60 min.	51.07	11.97	23.19	13.77
200°C/30 min.	61.34	8.47	19.31	10.88
200°C/60 min.	55.72	9.58	21.81	12.89

Table 3.4 XPS core level positions of $CH_3NH_3PbI_{(3-x)}Cl_x$ annealing at 150°C and 200°C in 30 minutes and 60 minutes.

Samples	Core level center (eV)							
	C 1s		Cl 2p		I 3d5		Pb 4f	
	1	2	1	2	1	2	1	2
150°C/30	287.18	285.30	199.93	198.24	619.63	617.92	143.65	142.29
150°C/60	286.70	285.06	199.73	198.17	619.21	618.04	143.86	142.65
200°C/30	286.70	285	199.65	198.18	619.37	617.98	143.54	142.42
200°C/60	286.44	285	199.67	198.13	619.76	618.30	143.81	142.67

the core level positions and full width at half maximum (FWHM) of the elements. Compared with the $CH_3NH_3PbI_{(3-x)}Cl_x$ powder, the The core level positions of C, Cl, Pb and I in $CH_3NH_3PbI_3$ and CH_3NH_3I are almost the same, again indicating the interactions between the elements are about the same in these three compounds.

Table 3.5 XPS core level positions of $CH_3NH_3PbI_{(3-x)}Cl_x$ annealing at 150°C and 200°C.

Samples	Core level center (eV)							
	C 1s		Cl 2p		I 3d5		Pb 4f	
	1	2	1	2	1	2	1	2
150°C/30 min.	2.00	2.00	1.40	1.46	1.40	1.40	1.32	1.46
150°C/60 min.	2.00	2.00	1.40	1.50	1.40	1.40	1.34	1.32
200°C/30 min.	2.00	2.00	1.40	1.40	1.61	1.62	1.42	1.42
200°C/60 min.	2.00	2.00	1.40	1.40	1.40	1.40	1.30	1.42
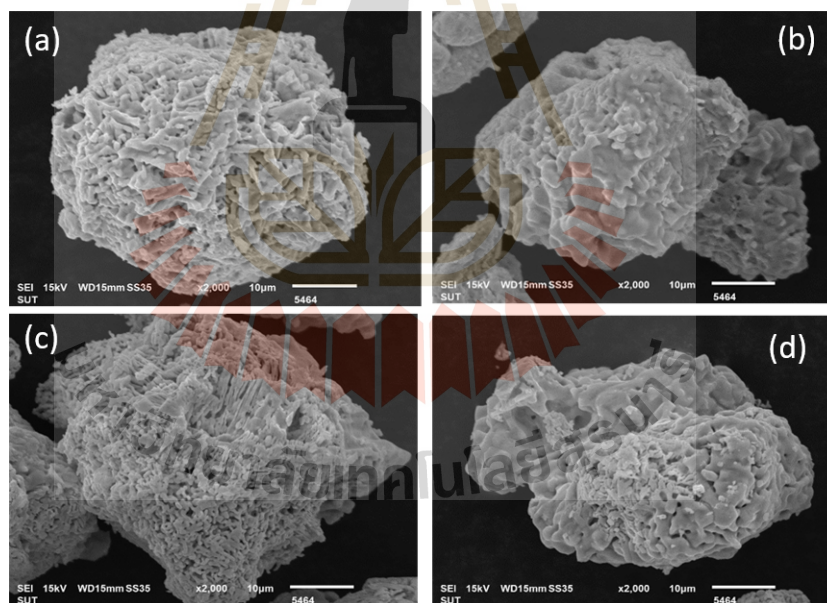
Figure 3.15 SEM image of the $CH_3NH_3PbI_{(3-x)}Cl_x$ powder surface on annealing at (a)150°C in 30 minutes (b) 150°C in 60 minutes (d) 200°C in 30 minutes and (d) 200°C in 60 minutes.

The SEM image of $CH_3NH_3PbI_{(3-x)}Cl_x$ powder in figure 3.15 shows the surface of powder not homogenous and has porous all of samples. There is a possibility that it is caused by organic salt of CH_3NH_3Cl that sticks on the skin. And we measured EDX for find present of element in surface the ratio of Pb and Cl are increasing when we increase temperature and I, N and C decreasing when we increase times to annealing (figure 3.16). And shows Spectrum of energy dispersive of $CH_3NH_3PbI_{(3-x)}Cl_x$ powder on annealing at 200°C in different times.
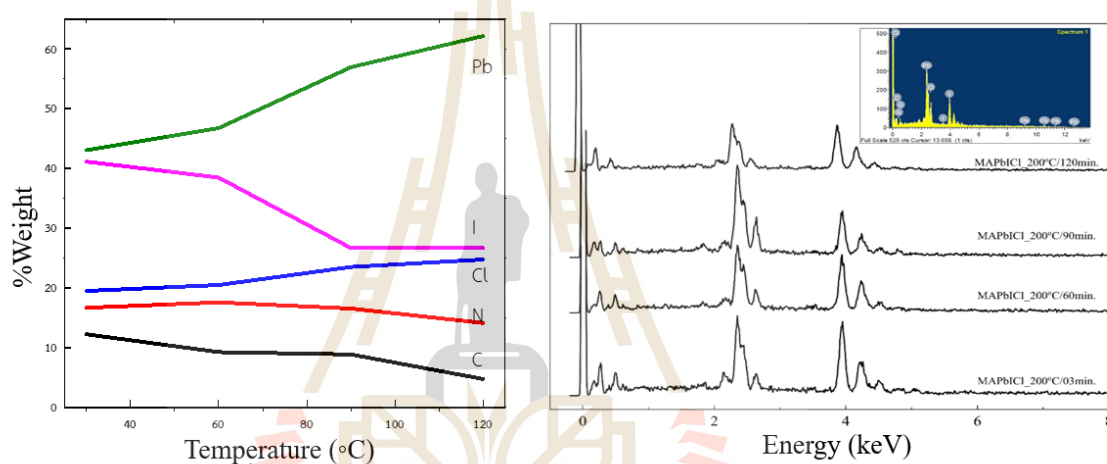
Figure 3.16 EDX trend and Spectrum of energy dispersive of the $CH_3NH_3PbI_{(3-x)}Cl_x$ powder surface on annealing at 200°C in different times.

The spectrum pattern of $CH_3NH_3PbI_{(3-x)}Cl_x$ and $CH_3NH_3PbI_3$ powder annealing at 200°C show in figure 3.17. The shape of spectra line is almost like to same in all of sample (difference of white line a little bit from PbI_2 precursor due to in $CH_3NH_3PbI_{(3-x)}Cl_x$ and $CH_3NH_3PbI_3$ powder have atom of MAI).That means atom of Iodide interact with Pb has a same of lattice structure (octahedral) for $CH_3NH_3PbI_{(3-x)}Cl_x$ and $CH_3NH_3PbI_3$ powder. And for normalized M_5 edge XANES spectra of Lead. The spectra feature of XANE are same of precursor because both of $PbCl_2$ and $CH_3NH_3PbI_{(3-x)}Cl_x$ are same of lattice structure (octahe-
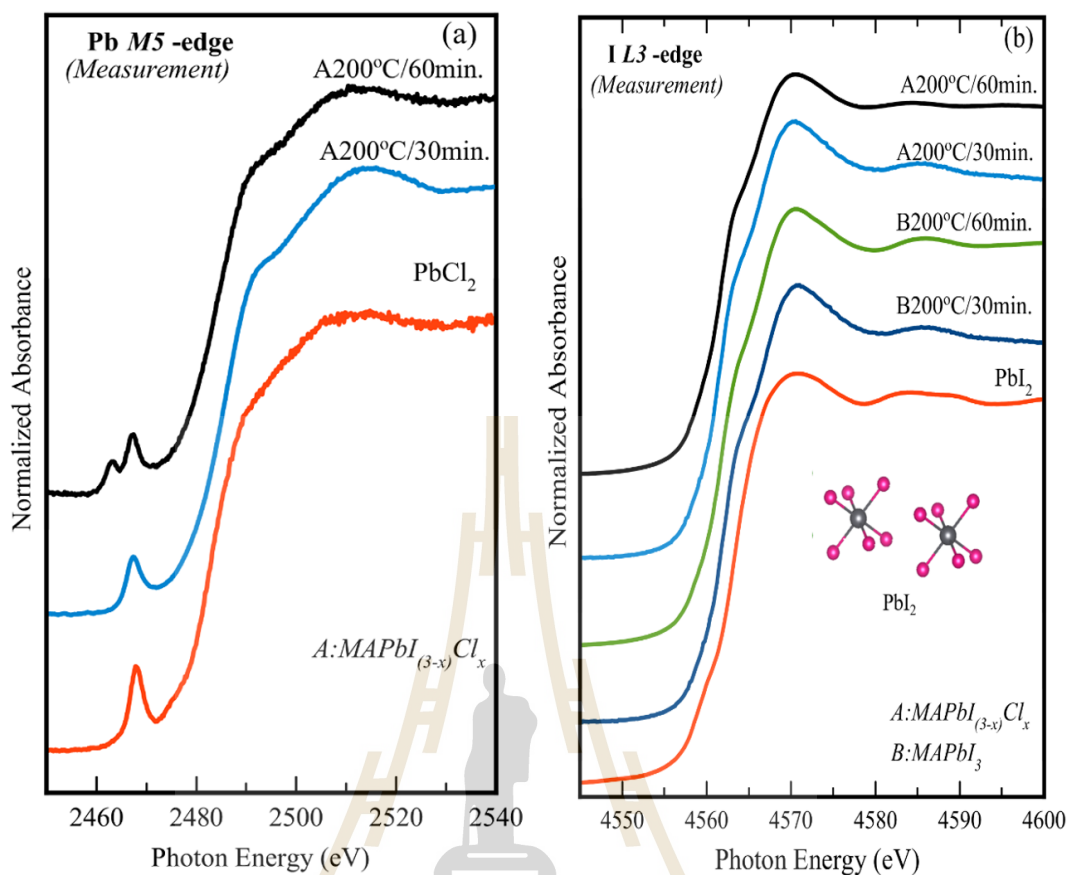
Figure 3.17 (a) Normalized L_3 edge XANES spectra of Iodide (b) Normalized M_5 edge XANES spectra of Lead for $CH_3NH_3PbI_{(3-x)}Cl_x$ powder.

dral). It possible that $PbCl_2$ is result of $CH_3NH_3PbI_{(3-x)}Cl_x$ decomposed or $PbCl_2$ is a excess reagent. The pre-edge region spectra of Lead in $CH_3NH_3PbI_{(3-x)}Cl_x$ powder annealing at 200°C for 60 minutes have two peak because in this condition, there are structural will be changes from octahedral structure to another type.

At the normalized K edge XANES spectra of Cholide. The feature of spectra is not similar in white line curve indicated to a neighbor atom not same. So, we will calculate the position of Cl in this powder. Although Cl is smaller atom than Lead and energy for XAS measured are nearly. Then we will be measured in fluorescent mode. The data of XAS can calculated by use spectra in rang of XANE. From the figure 3.18 shown the linear combination fit we found the

different of structure of Chloride and now we doing to calculation the ratio of $CH_3NH_3PbI_{(3-x)}Cl_x$ perovskite and CH_3NH_3Cl in this material by using FEEF calculation. And from the pattern of XRD in figure 3.16 shown the secondary phase of MACl, $PbCl_2$ or $CH_3NH_3PbI_{(3-x)}Cl_x$. Then we will use this structure of all to calculated in FEFF XANE.
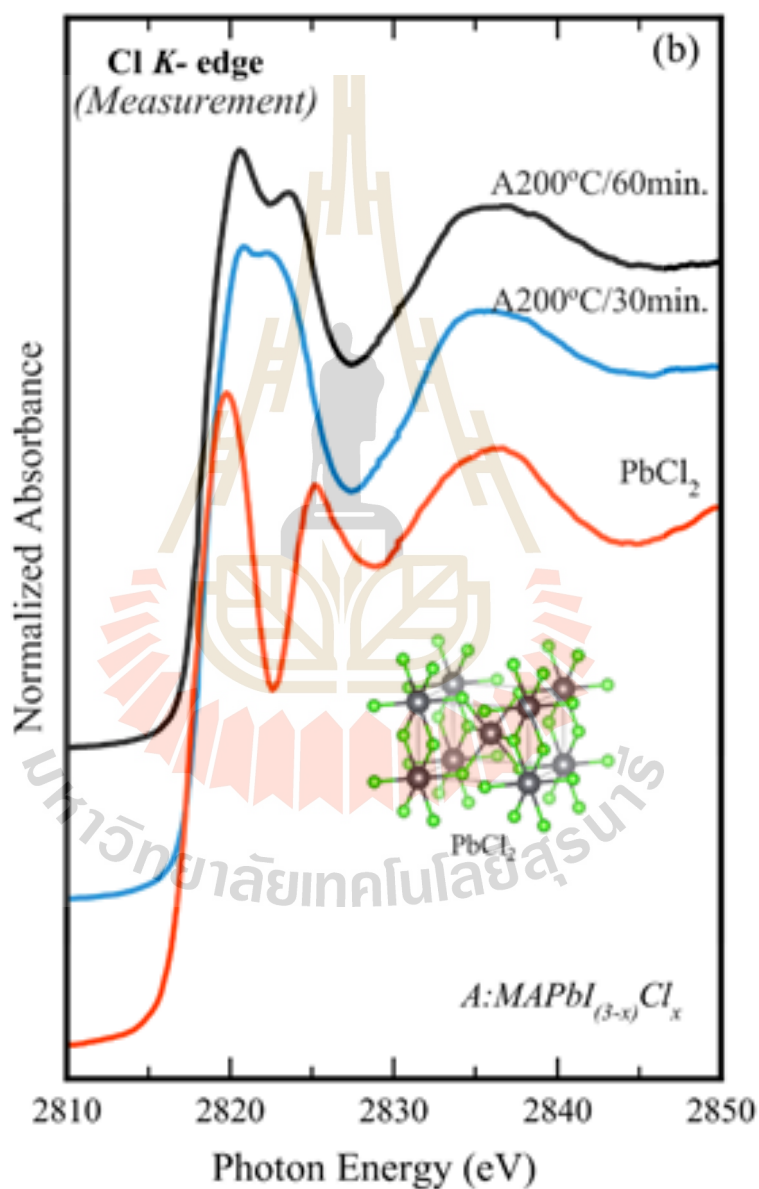
Figure 3.18 Normalized K edge XANES spectra of Chloride for $CH_3NH_3PbI_{(3-x)}Cl_x$ powder annealing at 200°C.
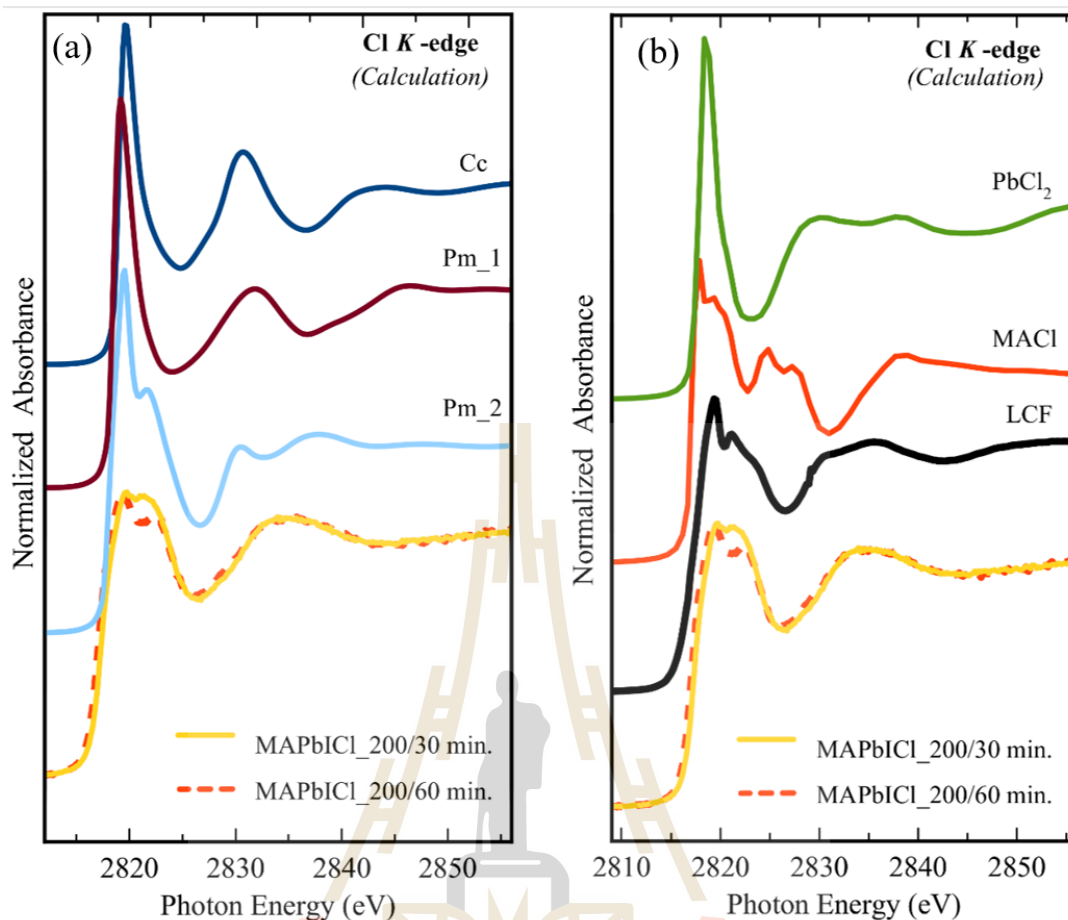
Figure 3.19 (a) Comparable of normalized K edge XANES spectra of Chloride for $CH_3NH_3PbI_{(3-x)}Cl_x$ powder annealing at 200°C with a structure of perovskite for FEFF XANE calculation. (b) Linear combination fit of normalized K edge XANES spectra of Chloride for $CH_3NH_3PbI_{(3-x)}Cl_x$ powder annealing at 200°C with $PbCl_2$, MACl from the calculation.

The figure 3.19(a) shows the possibility of perovskite structure and we choose this structure for FEFF XANE calculation. We compared normalized K edge XANES spectra of Chloride for $CH_3NH_3PbI_{(3-x)}Cl_x$ powder annealing at 200°C with the structure of perovskite by FEFF XANE calculation. And calculate the ratio of impossible structure in table 3.6 from linear combination fit in ATHENA program. The information from table 3.6 is just a trend of perovskite

structure because we used a data base of XRD of structure from the material project. We calculated XANES spectra of Chloride in linear combination fit in the range of -10 to 60 from edge step in figure 3.19(b). The result of a measurement is followed by possible chemical reactions involved in the perovskite formation process from precursor (MAI: $PbCl_2$) molar of ratio 3:1 (Pan et al., 2016) shows in table 3.6

Table 3.6 The data from linear combination fitting of $CH_3NH_3PbI_{(3-x)}Cl_x$ in spectra of Chloride with structure of perovskite for FEFF XANE calculation.

Structure type	Time and temperature to annealing	
	30 min./200°C	60 min./200°C
Pm_1	38.0	35.1
Pm_2	61.8	59.6
Cc	17.6	20.1
$PbCl_2$ Calculation	52.1	53.2
MACl Calculation	47.9	46.8

The data from table 3.7 represent to the constrain ratio of Cl in structure of $PbCl_2$ increasing when we increase time to annealing and for MACl decreased when increase time to annealing due to MACl can evaporate in lower temperature than $PbCl_2$ and in figure 3.19 the shape of peak indicate about possibility of Cl formation in MACl and $PbCl_2$.

Table 3.7 The data from linear combination fitting of $CH_3NH_3PbI_{(3-x)}Cl_x$ in normalized K edge XANES spectra of Chloride with $PbCl_2$ and MACl from calculation.

Structure type	Time and temperature to annealing	
	30 min./200°C	60 min./200°C
$PbCl_2$ Calculation	52.1	53.2
MACl Calculation	47.9	46.8

Monoclinic (Pm_2)   Orthorhombic (Pmna)   Monoclinic (Pm_1)   Monoclinic (Cc)

Cl
I
Pb
C
N
H
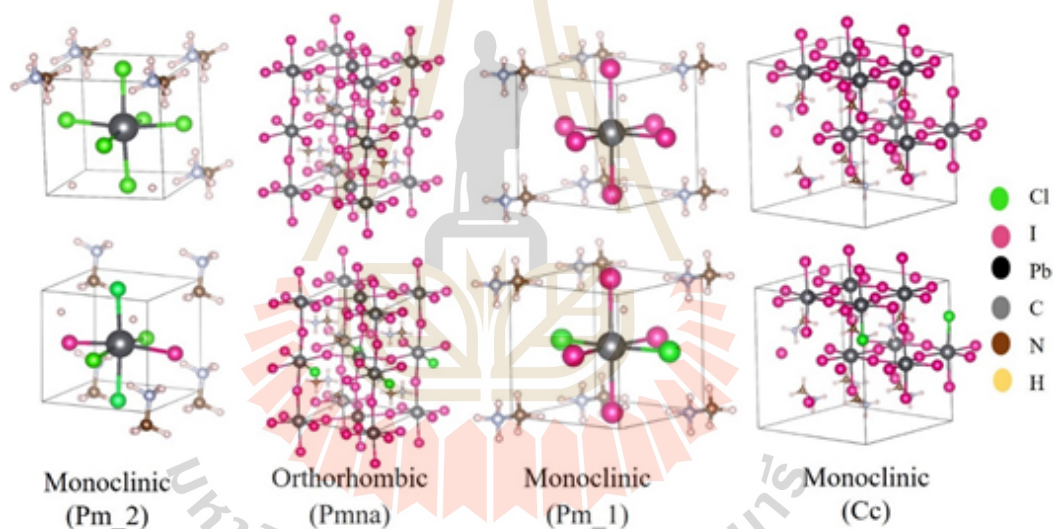
Figure 3.20 The data from linear combination fitting of $CH_3NH_3PbI_{(3-x)}Cl_x$ in spectra of Chloride with structure of perovskite for FEFF XANE calculation.

CHAPTER IV

STANDARD CHARACTERIZATION

RESULTS AND DISCUSSIONS

The CH_3NH_3I power precursors from different solvents were used to synthesis hybrid perovskite $CH_3NH_3PbI_3$ powders by solid state method with varying conditions. From the result of characterization comparable between CH_3NH_3I power washed by acetone and dry in Ar and CH_3NH_3I dissolved in diethyl ether after that precipitation in N, N-dimethylformamide (DMF) shown that the quality of hybride perovskite $CH_3NH_3PbI_3$ powders thus confirm the effective of the new preparation route and found that the synthesis time for MAI synthesis can be shorten by four times from dimethylformamide (DMF) to acetone. From the result of XRD and XAS, After that we synthesized $CH_3NH_3PbI_{(3-x)}Cl_x$ from difference ratio of precursor, vary times and temperature and characterized materials. From the result of XRD and XAS. we found Cl can't be substituted for I in the X side structure of perovskite (ABX_3) by solid state methods.
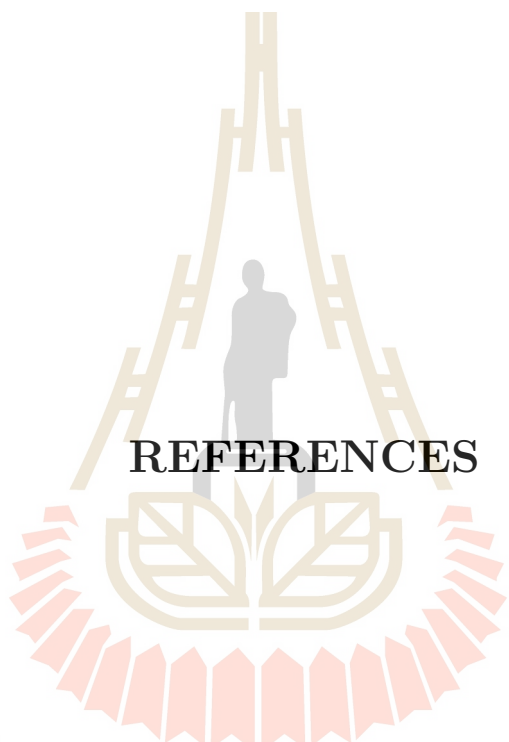
REFERENCES

REFERENCES

Administration, U. E. I. (2015). EIA projects 28% increase in world energy use by 2040. **International Energy Outlook 2017.**

Danad, I., Fayad, Z. A., Willemink, M. J., and Min, J. K. (2015). New applications of cardiac computed tomography: dual-energy, spectral, and molecular ct imaging. **JACC: Cardiovascular Imaging.**, 8(6): 710–723.

Elseman, A. M., Sajid, D. W., Shalan, A. E., Rashad, M. M., and Li, M. (2018). Pathways towards high-stable, low-cost and efficient perovskite solar cells. **Emerging Solar Energy Materials.**, page 201.

Essig, S., Allebé, C., Remo, T., Geisz, J. F., Steiner, M. A., Horowitz, K., Barraud, L., Ward, J. S., Schnabel, M., and Descoeudres, A. (2017). Raising the one-sun conversion efficiency of III–V/Si solar cells to 32.8% for two junctions and 35.9% for three junctions. **Nature Energy.**, 2(9): 17144.

Frost, J. M., Butler, K. T., Brivio, F., Hendon, C. H., Van Schilfgaarde, M., and Walsh, A. (2014). Atomistic origins of high-performance in hybrid halide perovskite solar cells. **Nano letters.**, 14(5): 2584–2590.

Green, M. A., Emery, K., Hishikawa, Y., Warta, W., and Dunlop, E. D. (2015). Cell efficiency tables (version 45). **Prog Photovoltaics: Res Appl.**, 23(1): 1–9.

Inc, S. (2018). XAS x-ray ABSORPTION SPECTROSCOPY system. **Quantum Leap Brochure.**

Jeon, N. J., Noh, J. H., Kim, Y. C., Yang, W. S., Ryu, S., and Seok, S. I. (2014). Solvent engineering for high-performance inorganic–organic hybrid perovskite solar cells. **Nature materials.**, 13(9): 897.

Levchuk, I., Hou, Y., Gruber, M., Brandl, M., Herre, P., Tang, X., Hoegl, F., Batentschuk, M., Osvet, A., and Hock, R. (2016). Deciphering the role of impurities in methylammonium iodide and their impact on the performance of perovskite solar cells. **Advanced Materials Interfaces.**, 3(22): 1600593.

Li, Y., Cooper, J. K., Buonsanti, R., Giannini, C., Liu, Y., Toma, F. M., and Sharp, I. D. (2015). Fabrication of planar heterojunction perovskite solar cells by controlled low-pressure vapor annealing. **The journal of physical chemistry letters.**, 6(3): 493–499.

Liu, L., McLeod, J. A., Wang, R., Shen, P., and Duhm, S. (2015). Tracking the formation of methylammonium lead triiodide perovskite. **Applied Physics Letters.**, 107(6): 061904.

McLeod, J. A., Wu, Z., Sun, B., and Liu, L. (2016). The influence of the i/cl ratio on the performance of ch 3 nh 3 pbi 3- x cl x-based solar cells: why is ch 3 nh 3 i: Pbcl 2= 3: 1 the "magic" ratio? **Nanoscale**, 8(12): 6361–6368.

Niu, G., Guo, X., and Wang, L. (2015). Review of recent progress in chemical stability of perovskite solar cells. **Journal of Materials Chemistry A.**, 3(17): 8970–8980.

Noel, N. K., Abate, A., Stranks, S. D., Parrott, E. S., Burlakov, V. M., Goriely, A., and Snaith, H. J. (2014). Enhanced photoluminescence and solar cell performance via lewis base passivation of organic–inorganic lead halide perovskites. **ACS nano.**, 8(10): 9815–9821.

Oku, T. (2015). Crystal structures of ch₃nh₃pbi₃ and related perovskite compounds used for solar cells. **Solar Cells-New Approaches and Reviews.**, 1.

Pan, Y.-Y., Su, Y.-H., Hsu, C.-H., Huang, L.-W., and Kaun, C.-C. (2016). The electronic structure of organic–inorganic hybrid perovskite solar cell: A first-principles analysis. **Computational Materials Science.**, 117: 573–578.

Shao, Y., Xiao, Z., Bi, C., Yuan, Y., and Huang, J. (2014). Origin and elimination of photocurrent hysteresis by fullerene passivation in ch₃nh₃pbi₃ planar heterojunction solar cells. **Nature communications.**, 5: 5784.

Sharenko, A., Mackeen, C., Jewell, L., Bridges, F., and Toney, M. F. (2017). Evolution of iodoplumbate complexes in methylammonium lead iodide perovskite precursor solutions. **Chemistry of Materials.**, 29(3): 1315–1320.

Stranks, S. D., Eperon, G. E., Grancini, G., Menelaou, C., Alcocer, M. J., Leijtens, T., Herz, L. M., Petrozza, A., and Snaith, H. J. (2013). Electron-hole diffusion lengths exceeding 1 micrometer in an organometal trihalide perovskite absorber. **Science.**, 342(6156): 341–344.

Yu, H., Wang, F., Xie, F., Li, W., Chen, J., and Zhao, N. (2014). The role of chlorine in the formation process of "ch3nh3pbi3-xclx" perovskite. **Advanced Functional Materials.**, 24(45): 7102–7108.

Zhang, Z., Zhao, X., Wang, T., Zhao, Y., Shen, C., Trevor, M., and Li, M. (2014). Research progress of solar cells based on organic–inorganic hybrid perovskites methylamine lead halide. **Energy and Environment Focus.**, 3(4): 354–359.
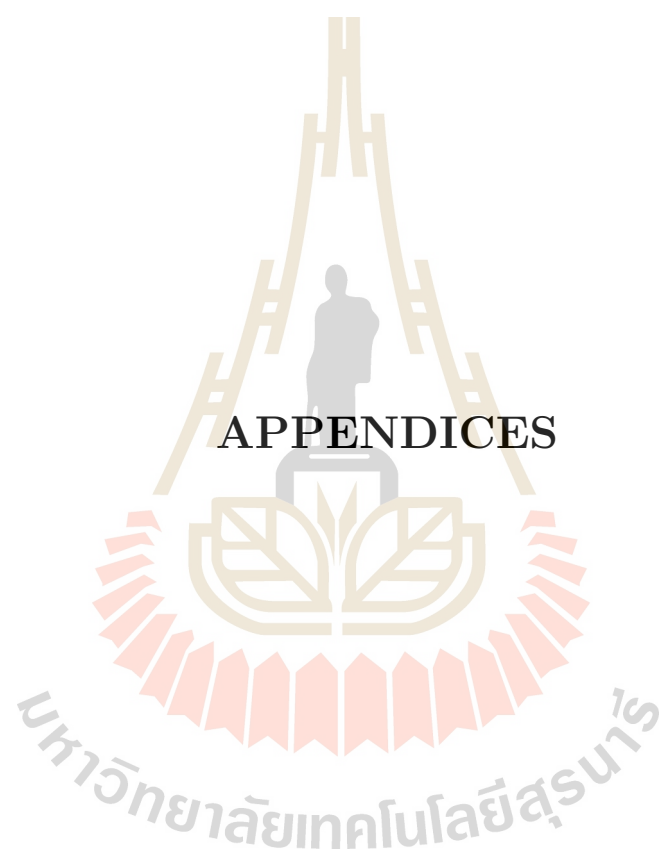
APPENDICES

Synthesis and characterization of $CH_3NH_3PbI_3$ and $CH_3NH_3PbI_{(3-x)}Cl_x$ perovskite solar cell materials

Phitsamai Kamonpha, Jintara Padchasri, Saroj Rujirawat, Usa Sukkha, Pinit Kidkhunthod, Narong Chanlek & Rattikorn Yimnirun

Abstract

The emerging of perovskite solar cell has attracted many interests in the synthesis and characterization of hybrid perovskite materials related to methylammonium iodide (MAI) due to various promising properties. In this work, we found a faster way to synthesize hybrid perovskite $CH_3NH_3PbI_3$ and $CH_3NH_3PbI_{(3-x)}Cl_x$ ($x = 0,1,2$) powders from a different solvent in the preparation process of MAI precursor. In addition, it was found that in $CH_3NH_3PbI_{(3-x)}Cl_x$ powders, as characterized by XRD and XAS, with a solid-state method employed Cl atoms cannot directly substitute for I in the perovskite (ABX_3) structure.

Keywords: Hybrid perovskite solar cell, XANES, MAI

The current status of time-resolved XAS beamline at SLRI and application on *in situ* experiments

Wanwisa Limphirat [a], Narinthorn Wiriya [b], Surangrat Tonlublao [a], Sarunyu Chaichoy [a], Piyawat Pruekthaisong [a], Suriya Duandmanee [c], Phitsamai Kamonpha [d], Dechmongkhon Kaewsuwan [d], Nonglak Meethong [b], Rungtiva P. Poo-arporn [e], Prayoon Songsiriritthigul [d], Josef Hormes [f], Yingyot Poo-arporn [a] ⊠

⊞ Show more

Abstract

Time-resolved X-ray absorption spectroscopy (TRXAS) beamline (BL2.2) was constructed to utilize a synchrotron radiation produced by a 1.2 T bending magnet from a 1.2 GeV storage ring at the Synchrotron Light Research Institute (SLRI), Thailand. The main optical component of the TRXAS beamline is an energy dispersive monochromator (EDM) which was donated by the University of Bonn, Germany. Using the energy-dispersive scheme with a position-sensitive detector, the beam size at the sample position can be small and have a fast detection speed in the XAS spectrum. At BL2.2, XAS measurement can be performed in the transmission mode using a 1024-pixel position-sensitive detector (PSD) and x-ray scintillator. Currently, the maximum measurable x-ray energy has been extended to 12 keV for the Pt L_3-edge EXAS measurement. Due to the advantages of the energy-dispersive setup, this beamline has focused on in-situ XAS experiments. In this review, the researchers summarize the developments of experimental tools to characterize catalysts, Li-ion batteries, and thin film using TRXAS to determine their electronic properties and structure under applied conditions.

Keyword: Synchrotron In-situ XAS Li-ion battery Catalyst Thin film

CURRICULUM VITAE

NAME: PHITSAMAI KAMONPHA   **GENDER**: Female

NATIONALITY: Thai   **DATE OF BIRTH**: MARCH 14, 1993

E-MAIL: phitsamai.own1993@gmail.com

EDUCATIONS:

- 2005 - 2010, High school at Buakhao school

- 2012 - 2015, Bachelor of Science,Physics department, Institute of science, Ubon Rachathani University

- 2016 - 2019. Master of Science, School of Physics, Institute of Science, Suranaree University of Technology

PUBLICATIONS

1. KAMONPHA, Phitsamai, et al. Synthesis and characterization of $CH_3NH_3PbI_3$ and $CH_3NH_3PbI_{(3-x)}$ Cl_x perovskite solar cell materials. Ferroelectrics, 2019, 552.1: 192-198.